Mixed layer heat and salinity budgets during the onset of the 2011 Atlantic cold tongue

Michael Schlundt[1], Peter Brandt[1], Marcus Dengler[1], Rebecca Hummels[1], Tim Fischer[1], Karl Bumke[1], Gerd Krahmann[1], and Johannes Karstensen[1]

[1]GEOMAR Helmholtz-Zentrum für Ozeanforschung Kiel, Kiel, Germany

Abstract The mixed layer (ML) temperature and salinity changes in the central tropical Atlantic have been studied by a dedicated experiment (Cold Tongue Experiment (CTE)) carried out from May to July 2011. The CTE was based on two successive research cruises, a glider swarm, and moored observations. The acquired in situ data sets together with satellite, reanalysis, and assimilation model data were used to evaluate box-averaged ML heat and salinity budgets for two subregions: (1) the western equatorial Atlantic cold tongue (ACT) (23°–10°W) and (2) the region north of the ACT. The strong ML heat loss in the ACT region during the CTE was found to be the result of the balance of warming due to net surface heat flux and cooling due to zonal advection and diapycnal mixing. The northern region was characterized by weak cooling and the dominant balance of net surface heat flux and zonal advection. A strong salinity increase occurred at the equator, 10°W, just before the CTE. During the CTE, ML salinity in the ACT region slightly increased. Largest contributions to the ML salinity budget were zonal advection and the net surface freshwater flux. While essential for the ML heat budget in the ACT region, diapycnal mixing played only a minor role for the ML salinity budget. In the region north of the ACT, the ML freshened at the beginning of the CTE due to precipitation, followed by a weak salinity increase. Zonal advection changed sign contributing to ML freshening at the beginning of the CTE and salinity increase afterward.

1. Introduction

Large-scale ocean-atmosphere interaction in the tropical Atlantic is an important driver of climate variability. It undergoes strong changes under current global warming conditions. Increasing sea surface temperatures (SSTs) [*Deser et al.*, 2010; *Xie et al.*, 2010] are associated with distinct changes in sea surface salinity (SSS) pattern [e.g., *Durack and Wijffels*, 2010], which were predicted by climate models as the result of an increased hydrological cycle [e.g., *Allen and Ingram*, 2002]. However, the physical processes dominating the oceans' heat and salinity balances in the mixed layer (ML), which interact with the overlying atmosphere, are often poorly understood. A particular phenomenon in the Eastern Equatorial Atlantic (EEA) is the annual development of a region of cold SSTs. This so-called Atlantic cold tongue (ACT) forms in boreal spring/summer, when the southeasterly trades intensify [*Philander and Pacanowski*, 1981], and retracts toward the end of the year resulting in uniformly warm SSTs within the tropical Atlantic. Minimum temperatures of about 22°C are reached within the "center" of the ACT at approximately 10°W [*Jouanno et al.*, 2011a]. This is a reduction of about 6°C compared to maximum SSTs occurring during late boreal winter and spring, before the onset of the ACT. The seasonal cycle of SST is most pronounced at this location. Toward the western and southern edges of the ACT, the seasonal cycle of SST is still evident, but temperatures do not reach the minimum values found at 10°W at the equator. The interannual variability of the SSTs within the ACT is small in amplitude compared to the seasonal cycle. Nevertheless, it is of climatic relevance: significant correlation was found between interannual variability of the ACT and the West African Monsoon (WAM) [*Brandt et al.*, 2011; *Caniaux et al.*, 2011].

The seasonal migration of the Intertropical Convergence Zone (ITCZ), in association with the corresponding wind field, is the most prominent phenomenon in tropical ocean-atmosphere interaction. In the EEA, the southeasterlies cross the equator throughout the year and the ITCZ is located to the north of the equator [*Philander et al.*, 1996]. The upper-ocean current system in the equatorial region is dominated by zonal flows: the eastward flowing Equatorial Undercurrent (EUC) and the westward South Equatorial Current (SEC)

at the sea surface. One consequence of the equatorial current structure is elevated vertical shear of horizontal velocity due to these opposing currents leading to elevated mixing in the upper thermocline [e.g., *Hummels et al.*, 2013]. Additionally, variability in the currents and in hydrography is caused by the passage of Tropical Instability Waves (TIWs), propagating westward at and near the equator [*Duing et al.*, 1975; *Legeckis*, 1977]. These waves are generated via barotropic and baroclinic instabilities of the zonal current system [*Philander*, 1978; *von Schuckmann et al.*, 2008].

A number of different processes lead to spatial and temporal variability of upper-ocean temperatures and salinities on diurnal, intraseasonal, seasonal, interannual, and longer time scales. Besides atmospheric forcing and horizontal advection through the currents, the ML is also influenced by vertical entrainment and diffusion through the ML base. However, the role of the different processes in the ML heat and ML salinity (MLS) budgets is still under debate. For the western ACT region, *Foltz et al.* [2003] showed the importance of horizontal advection by evaluating the different terms of the ML heat budget at PIRATA (Prediction and Research Moored Array in the Tropical Atlantic) [*Bourles et al.*, 2008] buoy locations. However, the authors were not able to close the ML heat budget for the equatorial sites at 23°W and 10°W, similar to the majority of other studies conducted within the ACT region [e.g., *Wade et al.*, 2011]. They speculated that unaccounted diapycnal mixing at the base of the ML may contribute to their unexplained residual. This contribution was recently estimated by *Hummels et al.* [2013]. Using an extensive set of microstructure observations, they showed that indeed the diapycnal heat flux through the ML base is a dominant cooling term during ACT development on the equator at 10°W. This is also in general agreement with results obtained from ocean general circulation models as was recently reported by *Jouanno et al.* [2011a].

A distinct feature of the upper equatorial thermocline in the central and eastern tropical Atlantic is a pronounced seasonal cycle of salinity [*Kolodziejczyk et al.*, 2014]. During early boreal summer, saline water masses of the upper thermocline are transported eastward within the EUC to the African coast and recirculate westward within the SEC on both sides of the EUC. During mid-boreal summer, the velocity maximum of the EUC weakens and the equatorial subsurface salinity maximum disappears [*Gouriou and Reverdin*, 1992; *Hisard and Morlière*, 1973; *Johns et al.*, 2014; *Kolodziejczyk et al.*, 2014].

In analogy to the ML heat content variability, the MLS variability is driven by horizontal salinity (or freshwater) advection, vertical entrainment at the ML base, surface freshwater flux (here defined as difference of evaporation and precipitation: E-P), and salinity diffusion. In fact, *Kolodziejczyk et al.* [2014] as well as *Johns et al.* [2014] recently suggested that intense mixing of the high-saline upper thermocline waters with surface waters in the eastern Gulf of Guinea (GG) is responsible for the erosion of the upper thermocline salinity maximum during late spring and summer. In general, the major difference in the evolution of ML heat and freshwater anomalies is the lack of a direct feedback between ocean and atmosphere for freshwater anomalies. Comparing the impact on density changes, the freshwater anomalies might be smaller in magnitude than heat anomalies, but their persistence can be longer [*Hall and Manabe*, 1997].

Analyses of the MLS budget in the western tropical North Atlantic indicated that horizontal advection dominantly contributes to the seasonal cycle in MLS [*Foltz and McPhaden*, 2008; *Foltz et al.*, 2004]. In the central and eastern tropical North Atlantic, seasonal variability is dominated by the seasonal cycle in precipitation [*Dessier and Donguy*, 1994; *Foltz and McPhaden*, 2008]. Similar results were found by *Da-Allada et al.* [2013] using a combination of in situ, satellite, and reanalysis data to constrain a simplified ML model. They showed that horizontal advection, entrainment, and precipitation dominantly contribute to the MLS variability in the eastern tropical Atlantic (ETA), in the GG, and in the Congo region (CO). In their study, the contribution of diapycnal mixing to the MLS budget was not considered due to a lack of observational data.

Recently, ocean remote sensing has yielded a large increase in available SSS data, particularly important to study the SSS variability of open ocean regions which were so far insufficiently sampled in the past by research vessels, thermosalinographs on voluntary observing ships and Argo floats. Currently, two satellite missions monitoring SSS are operating in parallel, namely the Soil Moisture Ocean Salinity (SMOS) mission of the European Space Agency [*Berger et al.*, 2002; *Font et al.*, 2012], which started in November 2009, and the joint U.S./Argentinean Aquarius/Satélite de Aplicaciones Científicas (SAC)-D mission [*Lagerloef et al.*, 2008], which started in June 2011. The high-resolution SSS data have provided new insights into oceanic freshwater cycles as well as surface ocean dynamics [e.g., *Lee et al.*, 2012; *Alory et al.*, 2012; *Tzortzi et al.*, 2013] and can be used to improve estimates of the MLS budget.
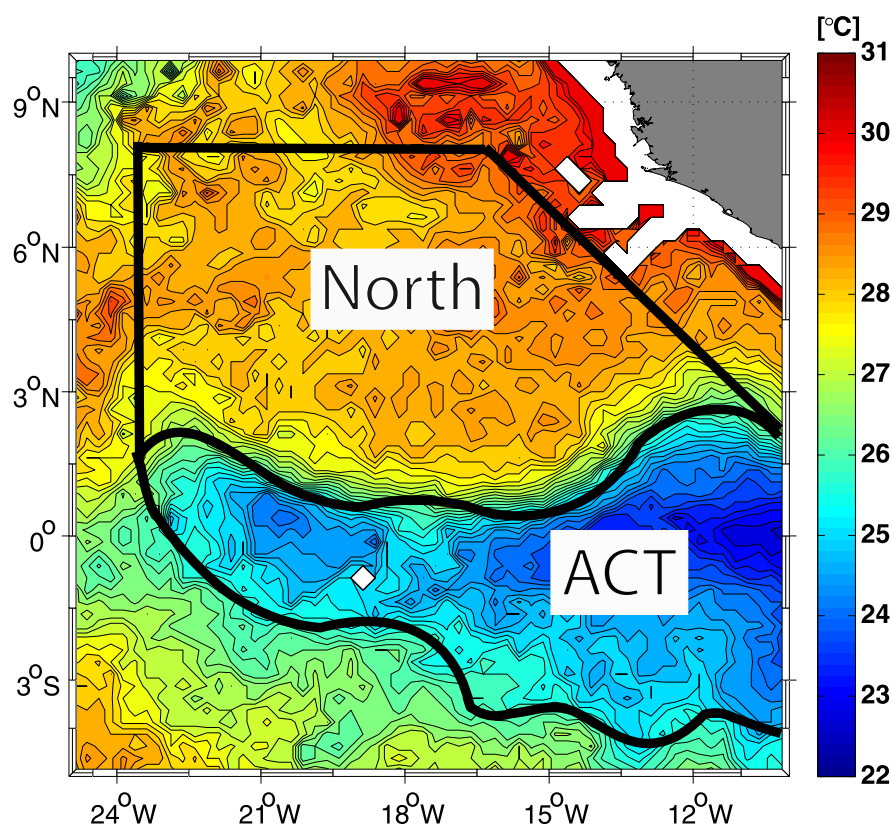
Figure 1. Box edges (black lines) and SSTs from TMI (background colors) between 14 and 17 June 2011. "ACT" describes the area associated with the Atlantic cold tongue (ACT box), while the northern box is denoted "North."

In this study, an extensive in situ data set is used to investigate the ML heat and salinity budgets concurrently. Hydrographic, oceanic microstructure, and atmospheric data collected during two expeditions on R/V Maria S. Merian (MSM) in spring/summer 2011 have been combined with simultaneous high-resolution temperature and salinity data from a glider swarm experiment. During this glider swarm experiment, six gliders were deployed to measure hydrographic properties between 2°S and 2°N (one glider track was extended to 4°S) and between 23°W and 10°W. In the following, we refer to the observational experiment as the "Cold Tongue Experiment" (CTE). The CTE data set is further augmented by temperature and salinity profiles from Argo floats and time series from PIRATA buoys and subsurface moorings.

In contrast to former studies, which concentrated on single mooring locations or empirically defined boxes and examined seasonal ML heat budgets [*Foltz et al.*, 2003; *Hummels et al.*, 2013; *Jouanno et al.*, 2011a; *Peter et al.*, 2006; *Wade et al.*, 2011], seasonal MLS budgets [*Da-Allada et al.*, 2013], seasonal SST variability [*Carton and Zhou*, 1997], or seasonal SSS variability [*Bingham et al.*, 2012; *Dessier and Donguy*, 1994], this study aims to estimate all terms contributing to the ML heat and MLS budgets as an average over the entire region associated with the western ACT (Figure 1). Due to the amount of ship time required to obtain such an extensive in situ data set, the CTE covers only 2 months of the year 2011. The CTE was scheduled between May and July to focus on the processes responsible for the variability of SST and SSS during the development phase of the ACT.

The paper is structured as follows. After describing the general approach, we present the data and the detailed methods in section 2. In section 3, we derive and combine the relevant contributions to the ML heat and salinity budgets and compare the results with mean seasonal cycles. A conclusion is presented and possible error sources are discussed in section 4.

2. Data and Methods

To determine the various components of the ML heat and salinity budgets, observations of various parameters were required at adequate resolution, i.e., data for all heat and freshwater flux components between
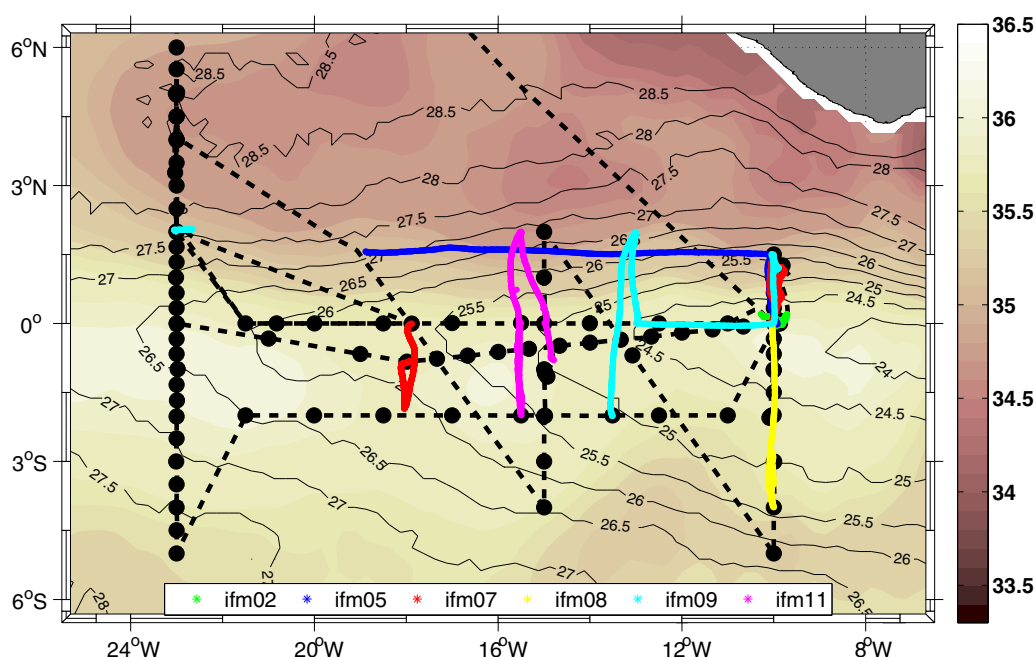
Figure 2. Observations during the cold tongue experiment conducted between May and July 2011. Colored lines denote the glider tracks, dashed black lines show cruise tracks, and black dots are CTD stations. Background colors show 3 month mean SSS from SMOS with contour interval 0.1, while contour lines show 3 month mean SST from TMI in °C. Contour interval is 0.5°C.

atmosphere and ocean, microstructure data to quantify oceanic mixing processes, ocean velocities, and the hydrography of the ML itself. The strategy pursued here, which is explained in more detail below, requires complementing the in situ database with further products, such as satellite observations, reanalysis products for ocean-atmosphere heat and freshwater fluxes, surface and ML velocities, and the output of a high-resolution assimilation model run. In this study, salinities are reported in practical salinity units (PSS-78).

2.1. Box-Averaging Strategy

In situ data collected during the CTE indicate that the ML within the ACT region is characterized by a relatively homogenous water mass. Elevated meridional temperature gradients limit the ACT region to the south between 3°S and 4°S and to the north between 1°N and 3°N. Maximum meridional temperature gradients from satellite SST at 3 day resolution were used to define the meridional extent of the ACT (Figure 1). The zonal boundaries of the ACT box were set to 23°W and 10°W based on the availability of ship and glider data. To compare the distinct characteristics of the heat and salinity budgets of the ACT region, a second box located to the north of the ACT between the northern ACT boundary and a fixed boundary at 8°N (Figure 1) was defined. Boxes used for the model analysis followed exactly the same approach. As detailed in Appendix A, all individual contributions to the ML heat and salinity budgets were calculated either from individual profiles or from a regular 1° × 1° grid and subsequently averaged in the two boxes.

2.2. Ship Data

During the two research cruises "MSM18/2" and "MSM18/3," lasting from the 11 May to the 11 July, profiles with a conductivity, temperature and depth (CTD) probe were acquired, as well as continuous observations of the upper-ocean temperature and salinity with a thermosalinograph (TSG) (Figure 2). CTD profiling was performed with a SeaBird 911 CTD rosette system and measured salinity was calibrated against bottle salinity samples analyzed with a Guildline Autosal salinometer. The TSG data were recorded every minute using a Sea-Bird 38/45 system with an intake located at 6.5 m depth in the front of the ship. The TSG observations were calibrated against CTD data from 6 to 7 m depth and later considered as additional ML temperature (MLT) and MLS observations for the box and time averaging and for the comparison with satellite observations.

Along with the CTD profiles, microstructure observations were performed at almost all stations. The microstructure data were collected using an MSS-90D profiler manufactured by Sea&Sun Technology. It was equipped with two shear sensors, a fast temperature sensor, an acceleration sensor, and a tilt sensor, plus a

set of slower response standard CTD sensors. The data were sampled at a rate of 1024 Hz. A detailed description of the probe is given in *Prandke and Stips* [1998]. From the observed velocity microstructure, it is possible to derive the dissipation rate of turbulent kinetic energy (TKE), from which the diapycnal fluxes of heat and salt can be estimated. The dissipation rate is calculated under the assumption of isotropic turbulence from the shear wave number spectrum ($E_{d\mathbf{u}'/dz}$). The spectrum is integrated between dynamically adapted wave number limits with $\varepsilon = 7.5\ v \int_{k_{min}}^{k_{max}} E_{d\mathbf{u}'/dz}(k)dk$ to estimate the dissipation rate ε (v is the kinematic viscosity of seawater). Due to the limited resolved wave number band, a variance loss correction is applied according to the universal Nasmyth spectrum [*Oakey*, 1982]. The derivation of dissipation rates followed here is described in detail in *Schafstall et al.* [2010] and *Hummels et al.* [2013].

Shipboard observations of atmospheric properties during CTE included measurements of the downward shortwave radiation flux with a pyranometer and the downward longwave radiation flux with a pyrgeometer every 2 s (for a description of the devices and the data processing see *Kalisch and Macke* [2012]). Precipitation was monitored using an optical disdrometer [*Großklaus et al.*, 1998] and the ship's rain gauge [*Hasse et al.*, 1998]. A description of the analysis inferring precipitation from the ship's rain gauge is given by *Bumke and Seltmann* [2012]. The reflected shortwave radiation was computed according to *Taylor et al.* [1996], while upward longwave radiation ($F^{\uparrow}_{LW}$) was calculated according to the Stefan-Boltzmann law, $F^{\uparrow}_{LW} = 0.97 \sigma SST^4$, where σ is the Boltzmann constant, assuming an emissivity of 0.97 for the sea surface. Turbulent heat fluxes and evaporation were computed from the ship's weather station data by using the parameterization of *Bumke et al.* [2014]. They estimated the bulk transfer coefficients for latent and sensible heat and the drag coefficient with the inertial dissipation method and compared their fluxes with the fluxes estimated with the latest version of the COARE algorithm [*Fairall et al.*, 2003] (Matlab program codes cor3_0af.m and cor3_0ah.m, available from ftp://ftp1.esrl.noaa.gov/users/cfairall/bulkalg/cor3_0/matlab3_0/). We also calculated the turbulent fluxes and the evaporation with the COARE algorithm, which yielded only marginal differences in the final fluxes, similar to the findings of *Bumke et al.* [2014].

2.3. Glider Data
Six autonomously operating Slocum electric gliders provided temperature and salinity profiles at approximately 3–4 km horizontal resolution and to maximum depths of 800 m. Altogether, 10 glider deployments, mostly along meridional sections (Figure 2), were performed during the CTE, yielding in a total of about 5600 profiles. Thermal lag hysteresis in salinity calculations was corrected by applying the method of *Garau et al.* [2011], where four correction parameters are determined by minimizing the area between two temperature-salinity curves of successive CTD casts.

2.4. Auxiliary Data Sets
2.4.1. Hydrographic Data
Temperature and salinity profiles from Argo floats (provided by the U.S. Global Ocean Data Assimilation Experiment (USGODAE)) and time series of temperature and salinity from the moored PIRATA buoys (provided by the Pacific Marine Environmental Laboratory (PMEL)) were used to further supplement the hydrographic data set during the CTE as a part of a large hydrographic data set.

2.4.2. Atmospheric Data
Several atmospheric data products for the surface radiative and turbulent heat fluxes and the freshwater flux were compared. In particular, the data from the ERA-Interim reanalysis [*Dee et al.*, 2011] from the European Centre for Medium-Range Weather Forecasts (ECMWF) are available for the net shortwave radiation, net longwave radiation, latent and sensible heat flux, evaporation, and precipitation. They provide 12 hourly data at 0.75° resolution. The second product that provides all relevant surface fluxes is the NCEP2 reanalysis [*Kanamitsu et al.*, 2002] from the National Center for Environmental Prediction (NCEP) with daily fields at 1.875° resolution. All radiative and turbulent heat fluxes together with evaporation are also available from TropFlux [*Praveen Kumar et al.*, 2012] on a 1° grid in the tropics (30°S–30°N) and at daily resolution. On the same spatial and temporal resolution, latent heat flux and evaporation were taken from the Objectively Analyzed air-sea fluxes (OAFlux) data from Woods Hole Oceanographic Institute [*Yu et al.*, 2008]. All daily averaged data sets were compared with daily averages of onboard in situ observations (for details see Appendix B). Bias, standard deviation, and root-mean-square of the differences are shown in Table 1. The best agreement between the different radiative or turbulent fluxes and the ship-based observations was achieved with different data products. However, the best general agreement was found for the TropFlux

Table 1. Bias, Standard Deviation (std), and Root-Mean-Square of the Differences (rmsd) of Shipboard In Situ Observations and Reanalysis/Satellite Products for Evaporation (E), Latent Heat Flux (LHF), Sensible Heat Flux (SHF), Net Surface Shortwave Radiation (SSR), and Net Surface Longwave Radiation (SLR)[a]

	ERA-Interim		NCEP2		OAFlux		TropFlux	
	Bias ± std	rmsd	Bias ± std	rmsd	Bias ± std	rmsd	Bias ± std	rmsd
E	−0.6 ± 0.7	0.9	−0.7 ± 1.1	1.5	0.1 ± 0.7	0.7	−0.3 ± 0.7	0.8
LHF	−18.7 ± 21.0	26.3	−19.2 ± 31.5	40.2	0.2 ± 19.3	19.8	−7.2 ± 21.6	21.5
SHF	−2.9 ± 4.1	5.4	2.9 ± 4.5	5.2			0.1 ± 2.7	2.7
SSR	4.5 ± 24.9	24.9	28.4 ± 60.2	68.9			8.6 ± 34.4	34.6
SLR	−8.3 ± 8.0	10.5	−1.4 ± 15.1	15.0			−3.7 ± 9.6	9.6

[a]Unit for E is mm d^{-1} while the unit for LHF, SHF, SSR, and SLR is Wm^{-2}.

product and the turbulent heat fluxes, evaporation, as well as net surface shortwave and longwave radiation are in the following taken from the TropFlux product.

Precipitation estimates were taken from the Advanced Microwave Scanning Radiometer (AMSR-E) onboard the NASA Aqua spacecraft, from the TRMM Microwave Imager (TMI) onboard the Tropical Rainfall Measurement Mission (TRMM) satellite, as well as from the Special Sensor Microwave Imager Sounder (SSMIS) F17 onboard the DMSP satellite. From all three products, daily averages at a quarter-degree resolution were statistically compared against the direct shipboard observations with the method of *Bumke et al.* [2012]. The analysis revealed by taking the statistical parameters into account, that the AMSR-E satellite precipitation product was closest to the observations and it was finally chosen (for details see Appendix B).

2.4.3. SST and SSS Data

SST data were taken from the TMI onboard the TRMM satellite to calculate horizontal SST gradients required to estimate the advective contribution to the heat budget. The 3 day means on a spatial grid of a quarter degree were used for the comparison between satellite SSTs and in situ SST observations (Figure 3a; for details see Appendix C). A standard deviation of the differences between satellite and in situ SST of 0.52°C was taken as the uncertainty for the satellite SSTs.

Horizontal SSS gradients were calculated based on the SMOS data. SMOS SSS measurements on a 1° × 1° grid and with 10 day composites have, compared to Argo SSS, a current bias of ∼0.3–0.4 [*Boutin et al.*, 2012; *Reul et al.*, 2012]. Here we used the 3 day mean fields on a quarter-degree grid to compare the satellite SSSs with in situ SSS observations (Figure 3b; for details see Appendix C). For the satellite SSS, a standard deviation of the differences between satellite and in situ SSS of 0.34 was calculated, which is used as the uncertainty for the satellite SSS.
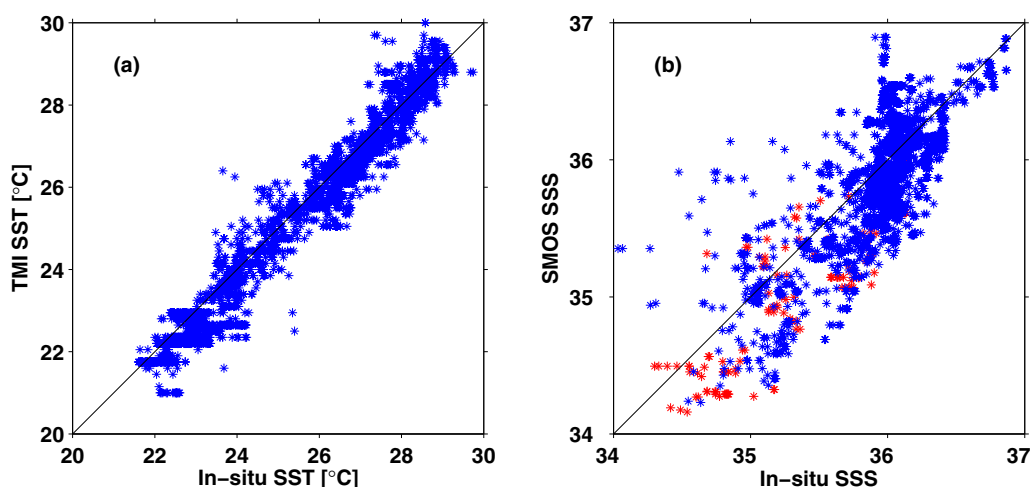

Figure 3. Scatterplot of (a) satellite SST with in situ SST and (b) satellite SSS with in situ SSS. Red dots in Figure 3b denote satellite grid points where SMOS observations coincide with precipitation (rain rate ≥ 0.1 mm h^{-1}) observations. The maximum distance between the closest satellite grid point and in situ measurement is ∼1/6° or ∼10 nm.
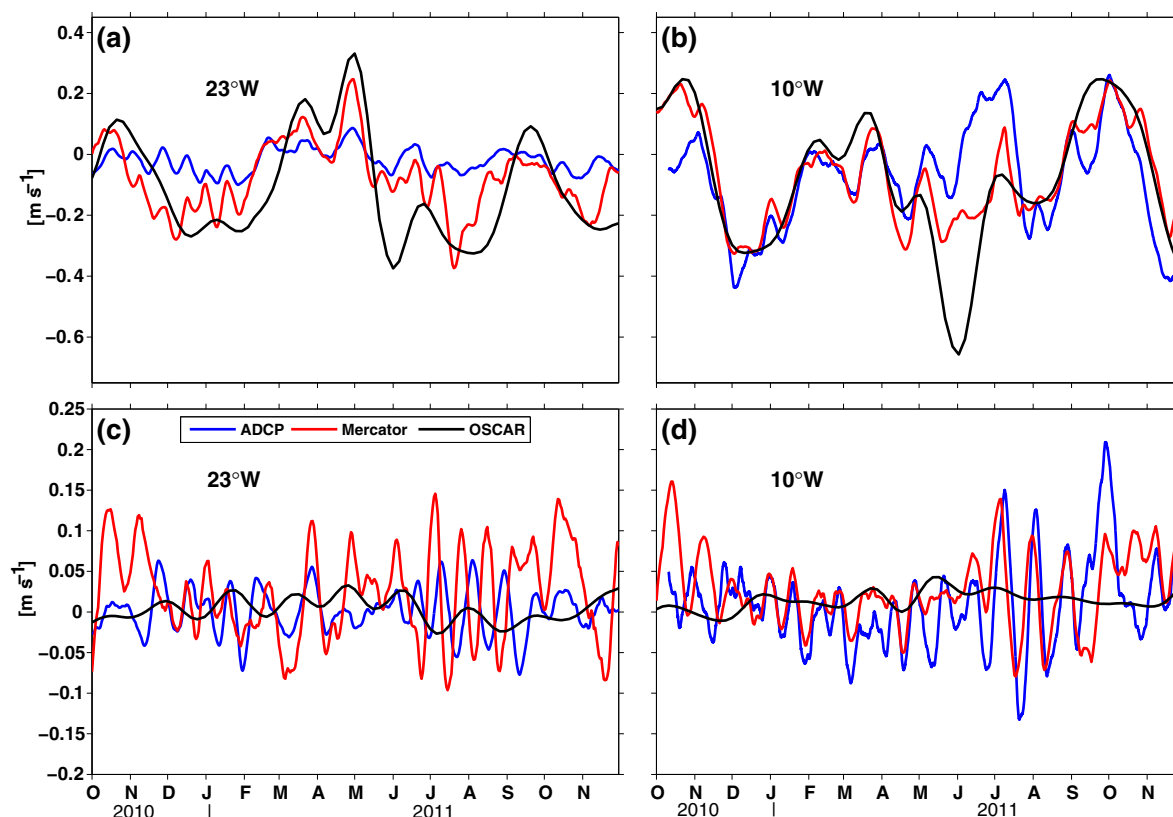
Figure 4. ML-averaged (a and b) zonal and (c and d) meridional velocities at the equator at 23°W (Figures 4a and 4c) and at 10°W (Figures 4b and 4d). The black line denotes the OSCAR product and the red line is the 5 day running mean Mercator estimate. The blue line denotes the 5 day mean subsurface ADCP-data.

2.4.4. Velocity Data

Surface velocities within the entire study region were required to estimate the advection terms. The Ocean Surface Current Analysis Real-time (OSCAR) product is used, which is derived from sea level measurements, wind stress, and SST data [*Lagerloef et al.*, 1999]. This data set represents vertically averaged geostrophic and Ekman velocities in the upper 30 m of the ocean [*Bonjean and Lagerloef*, 2002]. The filtered version of this data set at a horizontal resolution of 1° × 1° with a temporal resolution of 5 days is used here. Explanation and validation of the OSCAR product as well as error estimates are described in *Johnson et al.* [2007]. A comparison between OSCAR velocities and Moored Acoustic Doppler Current Profiler (mADCP) data at equatorial moorings (23°W and 10°W) is shown in Figure 4 and the analysis is described in Appendix D. *Foltz et al.* [2013] made a similar comparison between OSCAR velocities and moored velocities at 4°N, 23°W and their estimates of the uncertainties for the zonal and meridional velocity were used as the uncertainty in the northern box in this study. The comparison of OSCAR velocities with the mADCP velocities at the equatorial moorings at 23°W and 10°W showed larger variability of the zonal velocity component (Figures 4a and 4b) for the OSCAR product compared to mADCP velocities. OSCAR meridional velocities are instead weak (Figures 4c and 4d), indicating that the OSCAR product does not capture TIWs, which otherwise are clearly identifiable in the meridional component of the mADCP data.

2.4.5. Mercator Assimilation Model

In addition to the observation-based data products, we used the "Mercator Global operational System PSY2V4R2" model output in our analysis to estimate the horizontal advection terms and the entrainment. The model output corresponds to a simulation that assimilates SST and sea level anomaly (SLA) fields, temperature, and salinity profiles, and a mean dynamic topography. Three-dimensional fields of zonal and meridional velocities, temperature, and salinity are provided as output. The horizontal resolution is 1/12° × 1/12° (9 km at the equator; decreasing poleward) with daily fields. There are 36 vertical levels in the first

~1000 m. In the model, the vertical grid spacing changes from nearly 1 m close to the surface to about 150 m at 1000 m depth [*Lellouche et al.*, 2013].

Mercator velocities were compared to the OSCAR and mADCP data (Figure 4; see Appendix D). In contrast to OSCAR, the meridional velocities of Mercator capture TIWs (Figures 4c and 4d), which can have effects on the heat budget through horizontal eddy heat advection [*Foltz et al.*, 2003; *Giordani et al.*, 2013; *Jochum et al.*, 2007; *Peter et al.*, 2006]. However, particularly in the western cold tongue region, TIWs of the Mercator assimilation model were partly out of phase compared to observations (Figure 4c). Zonal velocities from OSCAR and the Mercator assimilation model showed some similarities, such as the same phase and amplitude of intraseasonal to seasonal signals, but had large differences as well (Figures 4a and 4b). In particular, the large westward OSCAR velocities during the CTE in the central cold tongue region (Figure 4b) are not present in the model output.

2.4.6. Data for the Mean Seasonal Cycles of MLS

The seasonal salinity budgets were estimated at the locations of three PIRATA buoys at the equator, 10°W and 23°W, and at 4°N, 23°W. A unique data set of microstructure shear and temperature profiles and CTD salinity profiles was used to estimate the dissipation rates of TKE. The data set was collected during nine cruises to the ACT region carried out in different seasons between 2005 and 2012. A detailed description of the data set and postprocessing procedures are given in *Hummels et al.* [2013, 2014]. For this study, the data set was supplemented by microstructure data from the R/V Maria S. Merian cruise MSM18/3. From this data set, profiles were used in the latitude range ±2° and in the longitude range ±0.3° relative to the nominal locations of the three selected PIRATA buoys.

All available buoy and mooring data, the essential database for this part of the study, from January 1999 to December 2012 (first dates used: 30 January 1999 for 0°N, 10°W; 7 March 1999 for 0°N, 23°W; 12 June 2006 for 4°N, 23°W) as well as several climatological products were used. Surface velocities were constructed from a combination of the YOMAHA'07 data set [*Lebedev et al.*, 2007] and available surface drifter trajectories [*Lumpkin and Garzoli*, 2005]. The YOMAHA'07 velocities were derived from Argo float trajectories and provided by the Asia-Pacific Data Research Center and the International Pacific Research Center (APDRC/IPRC). A detailed description of the wind-slip correction and the construction of the combined velocity product are given in *Perez et al.* [2014].

The horizontal salinity gradients were constructed from the global monthly mean salinity data set from the Japan Agency for Marine-Earth Science and Technology (JAMSTEC). This data set is derived from Argo float observations which are binned to 1° × 1° monthly means from January 2001 ongoing [*Hosoda et al.*, 2008]. We used the data until December 2012. The periods of data coverage from satellite observations of SSS, SMOS started in November 2009 and Aquarius in July 2011, are not long enough for a robust seasonal cycle.

Monthly means from AMSR-E precipitation (beginning in June 2002) and TropFlux evaporation (beginning in January 1999), and 3 day averages of SMOS SSS (beginning in January 2010) and TMI SST (beginning in January 2010), until December 2012 were used as well. The MLD climatology of *de Boyer Montégut et al.* [2004] was implemented to derive the horizontal gradients of the MLD. The MLDs were interpolated on a 1° × 1° grid and the gradients were estimated with central differences on that grid.

2.5. Methodology
2.5.1. Heat and Salinity Budgets

The ML heat balance can be expressed as follows [*Foltz et al.*, 2003; *Stevenson and Niiler*, 1983]

$$\rho c_p h \frac{\partial T}{\partial t} = -\rho c_p h \left(\boldsymbol{u} \cdot \nabla T + \overline{\boldsymbol{u}' \cdot \nabla T'} \right) - \rho c_p w_e \Delta T + q_0 + R. \tag{1}$$

T is the MLT, t is time, h is the MLD, $\boldsymbol{u}$ is the ML-averaged horizontal velocity, $\boldsymbol{u}'$ and T' are deviations from the temporal average (the temporal average is denoted with an overbar), $\Delta T = T - T_{-h}$ is the difference between T and the temperature at the base of the ML (T_{-h}), and w_e is the entrainment velocity. ρ is the density of the ML, c_p the specific heat capacity at constant pressure, and q_0 is the net heat flux through the ocean's surface corrected for the penetrative shortwave radiation through the ML base.

The local heat storage on the left-hand side of equation (1) is balanced by horizontal temperature advection (divided into a mean and an eddy part), entrainment into the mixed layer, net surface heat flux, and a

residual term R. The residual represents the sum of all unresolved physical processes and the accumulation of errors from the other terms. The net heat flux at the ocean's surface is the sum of the net (incoming minus reflected) shortwave radiation, corrected for the amount penetrating below the ML, the net longwave radiation, the latent heat flux, and the sensible heat flux.

Similarly, the balance for MLS is after, e.g., *Delcroix and Hénin* [1991] given by:

$$h\frac{\partial S}{\partial t} = -h\left(\boldsymbol{u}\cdot\nabla S + \overline{\boldsymbol{u}'\cdot\nabla S'}\right) - w_e\Delta S + (E-P)S + R. \tag{2}$$

S is the MLS, S' is the deviation from the temporal average, E is the evaporation, P is the precipitation, and $\Delta S = S - S_{-h}$ is the difference between S and the salinity at the base of the ML (S_{-h}). The first term on the right-hand side of equation (2) describes the horizontal advection of salinity (divided into a mean and an eddy part) and the second term represents salinity entrainment through the ML base. The third term is the freshwater flux through the ocean's surface, while R again represents the residual including the sum of all unresolved physical processes and the accumulated errors from the other terms.

According to *Stevenson and Niiler* [1983], the entrainment velocity can be defined as

$$w_e = H\left(\frac{\partial h}{\partial t} + w_{-h} + \boldsymbol{u}\cdot\nabla h\right). \tag{3}$$

The entrainment velocity thereafter is the sum of the local change in MLD with time, the vertical velocity w_{-h} at the ML base, and the horizontal advection of MLD ($\boldsymbol{u}\cdot\nabla h$). Only the upward movement (entrainment) in equation (3) was considered because downward movement (detrainment) does not affect the temperature or the salinity in the ML. This constraint was implemented with the use of the Heaviside unit function: $H(x) = (1, \ x \geq 0 \text{ and } 0, \ x < 0)$.

The different terms of equations (1) and (2) were estimated for the two boxes described in section 2.1 for the period of the CTE using 10 day time steps as well as for the PIRATA buoy sites at 4°N and the equator at 23°W and at the equator at 10°W using monthly averaged data. The different methodologies used to determine the individual contributions are described in the following.

2.5.2. Methodology to Derive Heat and Salinity Budget Terms
This section describes the calculation of the individual quantities and terms from equations (1) and (2). For all quantities, the calculation for the CTE is described at first and followed by the calculation for the mean seasonal cycles at the PIRATA buoys.

2.5.2.1. Mixed Layer Depth
The ML can be defined as the surface layer of constant potential density and hence the depth where the density starts to increase is the MLD. Another definition of the ML is a surface layer of constant temperature. Here, the depth where the temperature starts decreasing is called isothermal layer depth (ILD). The ILD was determined as the depth at which temperature is 0.5°C, lower than the temperature averaged between 2 and 6 m depth. The MLD was defined as the depth where the potential density has increased equivalently to a temperature decrease of 0.5°C while salinity and pressure are held constant. The required potential density increase was about 0.15 kg m^{-3}, slightly varying with SSS. We avoided effects of diurnal cycles in MLD/ILD for the temporal averaging of fluxes through the ML base by using these definitions. Diurnal cycles were present when using 0.2°C ILD-criterion (corresponding to a MLD-criterion of ∼0.06 kg m^{-3}). No significant difference between MLD and ILD was found in the high-resolution glider data at all locations. Therefore, the simpler temperature criterion was chosen for our definition of the MLD.

To estimate the seasonal cycles, the daily mean MLDs were averaged for all days of the year, using all available data from January 1999 to December 2012. Afterward, monthly means were constructed. From these, the temporal evolution of the MLD was calculated as well.

2.5.2.2. Horizontal Advection
For the CTE, horizontal advection was not separated into mean and eddy contribution, because the time period of the CTE was too short. Here, total advection of heat and salinity were estimated (1) by combining velocities from the OSCAR product with horizontal temperature and salinity gradients from satellites, respectively, and (2) from the Mercator assimilation model output. Horizontal gradients of satellite SST and SSS were calculated using central differences of the 1/4° gridded data set that were subsequently averaged

onto the OSCAR-native 1° × 1° grid. Finally, the 1° × 1° advection terms were spatially averaged for the two boxes described in section 2.1.

Velocities from the Mercator assimilation model were averaged in the upper 30 m using trapezoidal integration in order to be comparable to the OSCAR estimates. Advection of heat and salinity were then estimated on the 1/12° × 1/12° grid and subsequently averaged for the two boxes described above. Finally, the advective terms from the OSCAR/satellite product and from the model were temporally averaged over 10 days.

A comparison of the spatially averaged advection terms in the two boxes showed that zonal heat and salinity advection determined from the model output was smaller compared to those determined from the OSCAR/satellite product (not shown). The main reason for the difference is the generally weaker zonal velocity of the Mercator assimilation model output compared to the OSCAR estimates for the CTE period. This behavior is illustrated in Figures 4a and 4b for the equatorial PIRATA buoy sites at 23°W and 10°W representing the ACT box. The meridional heat and salinity advection as obtained from the OSCAR/satellite product and the model output shows smaller differences. Despite the strong difference of the meridional velocities as obtained from the OSCAR product and the model output, the resulting contribution of meridional advection to ML heat or salinity changes is small for both products.

To obtain a mean seasonal cycle of horizontal salinity advection, mean and eddy advection were calculated separately at the PIRATA buoy sites. For the mean salinity advection, monthly mean velocities were calculated on a 1° × 1° grid from all available float and drifter data. The monthly mean horizontal gradients of SSS from float observations were calculated with central differences on the same 1° × 1° grid and afterward averaged for the mean seasonal cycle. Note, that the salinity climatology captures only the time from January 2001 to December 2012.

Eddy salinity advection, ($\overline{\boldsymbol{u}' \cdot \nabla S'}$), was estimated for the equatorial moorings by assuming a correlation between temperature and salinity fluctuations. Using the eddy temperature advection ($\overline{\boldsymbol{u}' \cdot \nabla T'}$), the eddy salinity advection was calculated via

$$\overline{\boldsymbol{u}' \cdot \nabla S'} \approx \overline{\boldsymbol{u}' \cdot \nabla T'} \frac{\delta \boldsymbol{S}}{\delta \boldsymbol{T}}. \tag{4}$$

The eddy temperature advection is calculated indirectly as the residual of the mean horizontal advection, estimated with the mean TMI SST and the aforementioned mean velocities [*Hummels et al.*, 2014], and the total horizontal advection, estimated by the difference between total time derivative and local time derivative of SST [*Swenson and Hansen*, 1999]. The total time derivative of SST is calculated from SST changes along Lagrangian drifter trajectories. The local time derivative is estimated from monthly averaged TMI SSTs. The regression of SSS and SST ($\frac{\delta S}{\delta T}$) was calculated on a monthly basis by using 3 years (2010–2012) of 3 day averages of satellite SSS and SST observations in a box 2.5° × 2.5° around the buoy locations and daily PIRATA SSS and SST observations from 1999 to 2012. The regression coefficient for one climatological month is calculated separately for the satellite and the buoy observations by taking the slope of the regression line of all pairs of SSS and SST observations in the particular month in all years. Finally, the monthly mean of the monthly satellite and buoy regression coefficients are used. The two independent estimates of the regression of SSS and SST are very similar with regard to their seasonal cycle and their annual means (Table 2).

2.5.2.3. Entrainment

Entrainment was calculated from the Mercator assimilation model output only. There were no observational vertical velocity estimates available for the period of the CTE. The vertical velocity at the ML base was calculated using the continuity equation $w_{-h} = h(\nabla \cdot \boldsymbol{u})$. Horizontal gradients of ML velocity and MLD were estimated with central differences on the 1/12° × 1/12° model grid. Local changes in MLD were derived on a daily basis.

Entrainment for the mean seasonal cycles at the PIRATA buoy locations was calculated from the MLD gradients, the horizontal divergence of the monthly mean horizontal velocities and the local time derivative of the MLD.

2.5.2.4. Surface Heat and Freshwater Fluxes

All atmospheric data sets were regridded linearly on a 1° × 1° grid and for the surface freshwater flux combined with box and time-averaged MLS and MLD (Appendix A). The penetrative shortwave radiation was

Table 2. Annual Mean and Annual Standard Deviation of Regression Coefficients (in °C^{-1}) Between SSSs and SSTs[a]

	Satellite (SMOS/TMI)	PIRATA
0°N, 10°W	-0.25 ± 0.11	-0.21 ± 0.14
0°N, 23°W	-0.17 ± 0.09	-0.18 ± 0.17
4°N, 23°W	-0.12 ± 0.13	-0.27 ± 0.35

[a]Shown are the values for three mooring sites for satellite data and PIRATA buoy data.

calculated following *Wang and McPhaden* [1999], assuming an exponential decay of surface shortwave radiation with 25 m *e*-folding depth for the North box and 15 m for the ACT box. The smaller *e*-folding depth (i.e., stronger absorption of shortwave radiation) in the ACT region follows from enhanced chlorophyll concentrations near the equator [e.g., *Grodsky et al.*, 2008].

For the seasonal cycles of the surface freshwater flux, monthly means of all atmospheric data sets were used and averaged in mean months of the year. These were combined with monthly means of MLS and MLD estimated with the PIRATA buoy data.

2.5.2.5. Diapycnal Diffusivities and Fluxes
In regions where the stratification is dominated by temperature, the diapycnal diffusivities of heat and mass are similar ($K_h = K_\rho$, e.g., *Peters et al.* [1988]). Using the observed dissipation rates, the diapycnal diffusivity of mass was estimated following *Osborn* [1980]

$$K_\rho = \Gamma \varepsilon N^{-2}. \tag{5}$$

N^2 is the buoyancy frequency and Γ is the turbulent mixing efficiency. Γ is set constant to 0.2, which is commonly used in several other studies [e.g., *Moum et al.*, 1989; *Hummels et al.*, 2013]. Further, the diapycnal heat flux was estimated using

$$J_{heat} = -\rho c_p K_\rho \frac{\partial T}{\partial z}. \tag{6}$$

For shear-driven turbulence, the diapycnal diffusivity of salt (K_S) is equal to the diapycnal diffusivity of heat [e.g., *Osborn and Cox*, 1972; *Osborn*, 1980; *Schmitt et al.*, 2005] and, thus, equal to the diapycnal diffusivity of mass ($K_S = K_h = K_\rho$). With this assumption, the diapycnal salt flux was calculated using

$$J_{salt} = -K_\rho \frac{\partial S}{\partial z}. \tag{7}$$

Diapycnal diffusivities, vertical temperature gradients, and vertical salinity gradients were averaged vertically in this study between 5 and 15 m below the ML base. The upper boundary was chosen to exclude ML values from the average. *Lien et al.* [2008] and *Hummels et al.* [2013] showed that the diapycnal heat flux is highly divergent in the vertical and rapidly decreases below the ML base. Therefore, the average within the narrow layer between 5 and 15 m below the ML base was used. Due to the limited amount of microstructure profiles available and the large variability inherent in turbulent mixing in the ocean, diapycnal fluxes were averaged for two periods: (1) the first half of the CTE (May until mid-June) and (2) the second half of the CTE (mid-June/July). To these two periods will be referred later in section 3, when the ML budgets are described. For the seasonal cycles, monthly means of the diapycnal salt flux were calculated. Uncertainties of the fluxes were estimated from error propagation and boot strapping as detailed in *Hummels et al.* [2013].

2.5.2.6. Harmonic Fitting
Annual and semiannual harmonics were fitted to all monthly averaged data, which were used for the description of the seasonal cycles. The total error of the fit (err_{tot}) combines the data error (err_{data}) and the error estimated as the standard deviation between the data and the fit (err_{fit}) and is calculated with $err_{tot} = \sqrt{err_{data}^2 + err_{fit}^2}$. The data error consists of given uncertainties from the data provider and errors from averaging of daily or monthly data into monthly climatologies using error propagation.

3. Results

3.1. The ACT in Boreal Summer 2011
3.1.1. Surface Observations of Temperature and Salinity
The long-term observations of SST and SSS at the PIRATA buoy sites at 23°W and 10°W on the equator can be used to investigate the exact timing of ACT development during 2011 with respect to the climatological cycles (Figure 5). At 23°W (western part of ACT region), SST (Figure 5a) and SSS (Figure 5b) in 2011 align well with the average seasonal cycle. In contrast, in the center of the cold tongue at 10°W, the onset of the cooling was approximately 1 week earlier and the cooling was stronger in 2011 compared to the
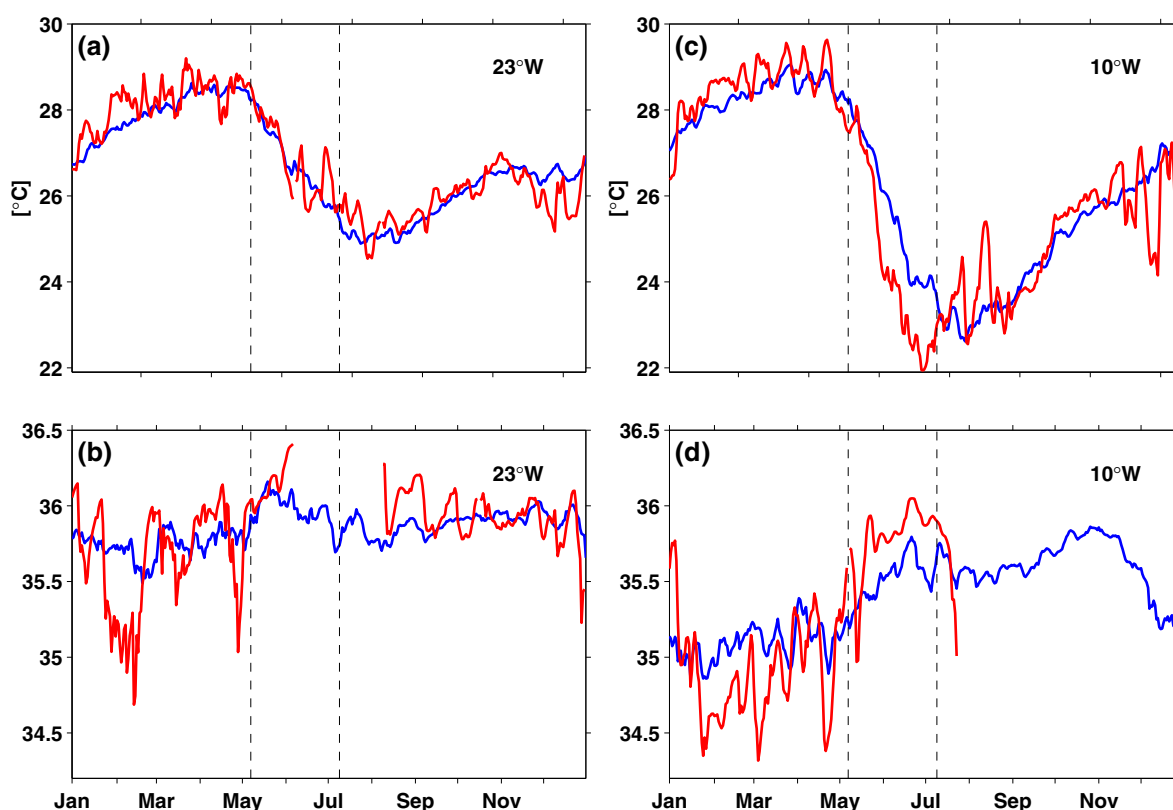
Figure 5. Mean seasonal cycle (blue) of (a and c) SST and (b and d) SSS for the PIRATA buoy at 23°W at the equator (Figures 5a and 5b) and 10°W at the equator (Figures 5c and 5d) based on averaging all data from beginning of the measuring period (SST/SSS at 23°W: 7 March 1999; SST at 10°W: 15 September 1997; SSS at 10°W: 29 January 1999) to the end of 2012. The red line indicates SST and SSS in 2011, while the dashed vertical black lines mark the beginning and end of the CTE.

climatology (Figure 5c). Similarly, SSS exhibited an earlier and stronger increase this year (Figure 5d). The comparison shows that the time period of our experimental campaign (May-July 2011) was well chosen in terms of studying the processes during cold tongue development as well as covering the entire cooling period in the center of the ACT. However, a large SSS increase occurred before the CTE that was not covered by our measurements.

The onset and spreading of the ACT in boreal summer 2011 is apparent in the monthly equatorial SST evolution (Figures 6a, 6c, 6e, and 6g). The strongest cooling, resulting in minimum temperatures of less than 22°C, was found at the equator at around 10°W. In June and July, the negative SST anomaly expanded further to the west- and southwest, but with a weaker intensity. The monthly satellite data showed a strong increase in SSS in the EEA from April to May (Figures 6b and 6d) followed by a period of nearly constant SSS (Figures 6f and 6h). Within the northern box (Figure 1), a reduction of SSS occurred from April through June, which is associated with the northward migration of the ITCZ. From June to July, SSS increased in the southern part of that region (2°N–5°N).

3.1.2. Vertical Structure of Temperature and Salinity

Subsurface hydrographic changes during ACT development at 10°W were monitored with high vertical and temporal resolution using glider (Figure 7) and moored temperature and salinity recorders. Surface cooling, as evident from the satellite SSTs, was also clearly visible in the gliders' CTD measurements (Figure 7a). In addition, the high vertical resolution of those data revealed a shoaling of the MLD during the first month of observations (Figure 7c).

The temporal evolution of the vertical salinity structure was more complex. At the beginning of the time series, a pronounced salinity maximum was present below a rather fresh ML (Figure 7b). The salinity maximum is related to the eastward transport of saline water from the western Atlantic within the EUC occurring during spring [Johns et al., 2014; Kolodziejczyk et al., 2014]. A strong increase in MLS was observed
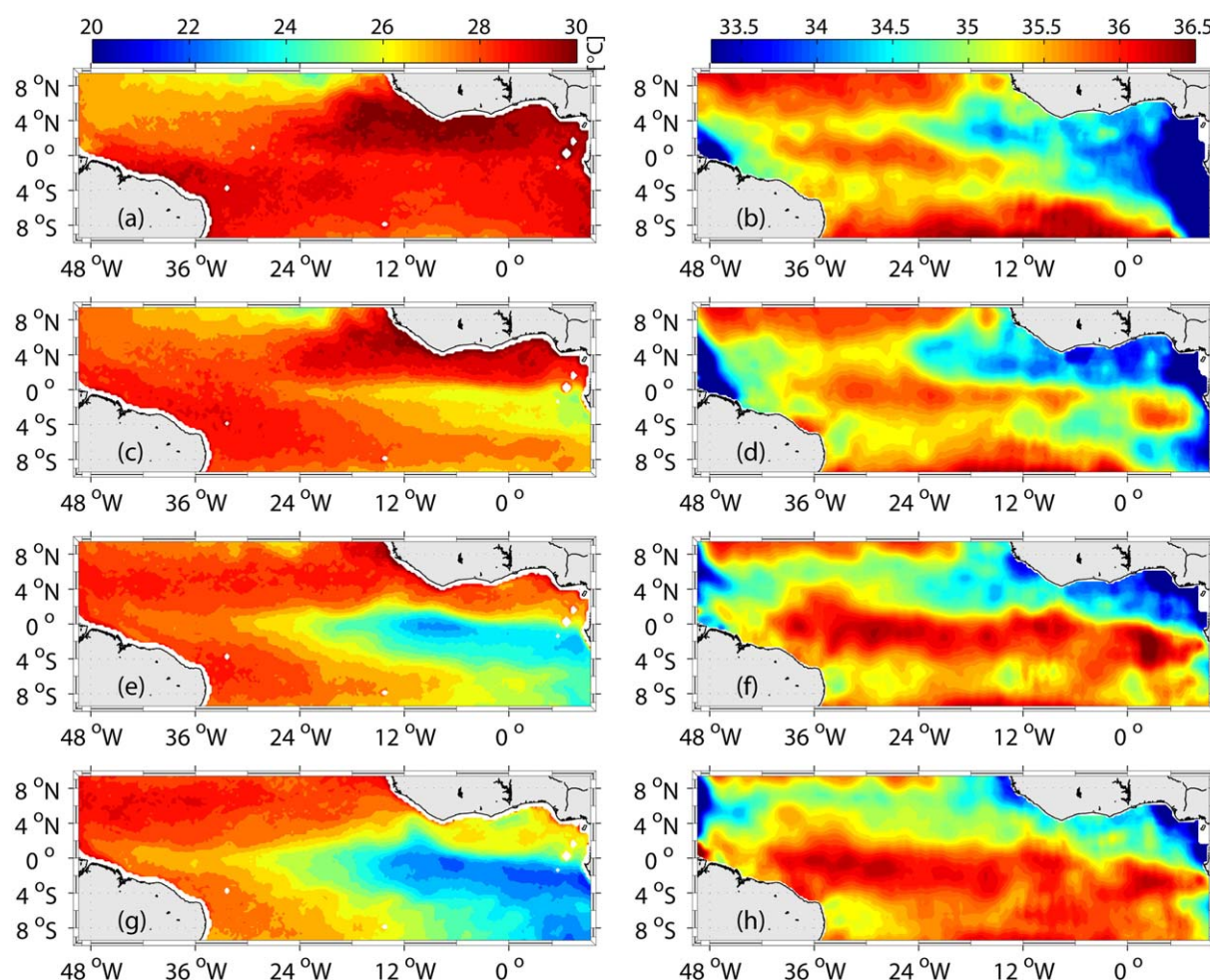
Figure 6. Monthly mean fields of SST (a, c, e, and g) from TMI and SSS (b, d, f, and h) from SMOS. Figures 6a and 6b are April, Figures 6c and 6d are May, Figures 6e and 6f are June, and Figures 6g and 6h are July.

with the onset of the cold tongue, while the subsurface salinity maximum was reduced. The simplest explanation would be a vertical redistribution and mixing of salinity through exchange processes across the ML base. However, advective processes played the dominant role as will be shown below. MLS remained elevated during the further development of the cold tongue, whereas in the beginning of July the subsurface salinity maximum reappeared. Typically, MLDs are shallowest in tropical upwelling regions [e.g., *de Boyer Montégut et al.*, 2007]. Indeed, at the survey site, MLD never exceeded 30 m, but a clear diurnal cycle is visible when using a smaller temperature criterion (dT = 0.2°C) for the MLD than chosen for the ML budgets, i.e., dT = 0.5°C (Figure 7c). The abrupt increase in MLT and decrease in MLS on 14 May (Figures 7a and 7b) was a remarkable event in the temperature and salinity time series, which counteracted the trends expected from the cold tongue development. Satellite SST distributions from this period (not shown) suggested that the anomaly was caused by the propagation of a TIW that moved the SST front, here defined as the maximum meridional SST gradient at 10°W, north of the ACT southward (Figure 7d).

The glider surveys along meridional or zonal sections (Figure 2) exhibit a mixture of temporal and spatial variability. One glider was assigned to profile along a meridional section at 15.5°W between 2°S and 2°N (Figure 8d). The glider crossed the SST front on 10 June, stayed north of the front, and crossed back on 18 June (Figure 8d). The first crossing of the front was clearly visible in the freshening of the ML in association with increased temperatures (Figures 8a and 8b). North of the front, a diurnal cycle in MLD (using the 0.2°C criterion) is not evident (Figure 8c). The glider was close to the equator and crossed the EUC core with the subsurface salinity maximum three times: at the beginning of the section, around the 10 June, and at the
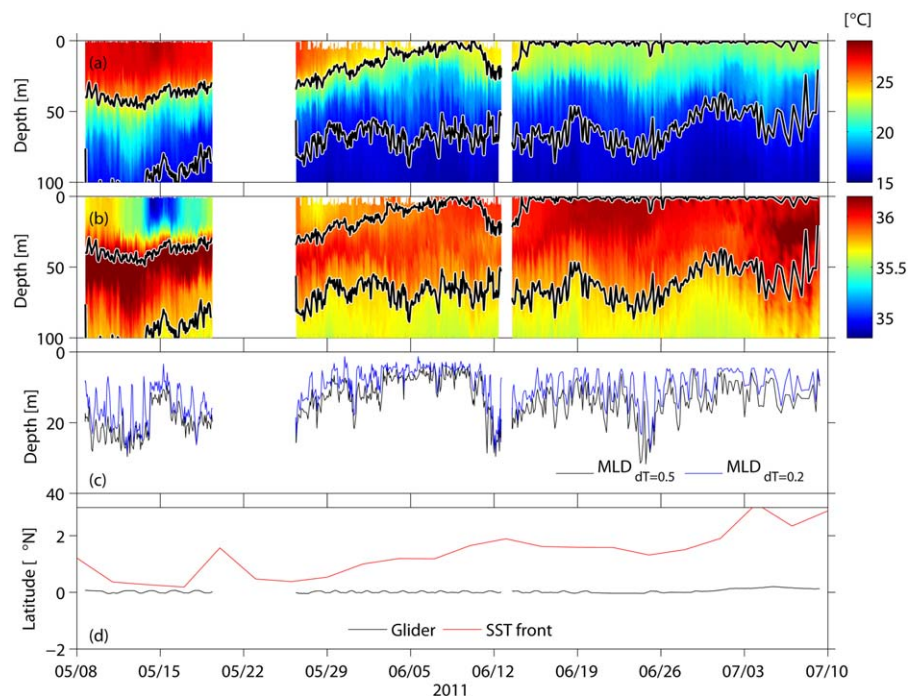
Figure 7. Time series of glider ifm02 of (a) temperature, (b) salinity, (c) MLD, and (d) latitudinal position (black). In Figures 7a and 7b, the potential density surfaces 24.5 and 26.2 are denoted in black. In Figure 7d, the latitude of the SST front at 10°W is denoted in red. The glider profiled close to the PIRATA buoy at 10°W all the time. The two gaps in the time series stem from recoveries for battery exchanges.

end of June (Figures 8b and 8d). North and south of the equator and away from the EUC, the subsurface salinity maximum was weak or not present.

To further investigate the spatial and temporal distribution and evolution of the subsurface salinity maximum, the glider and CTD data were supplemented with CTD data from a French PIRATA cruise
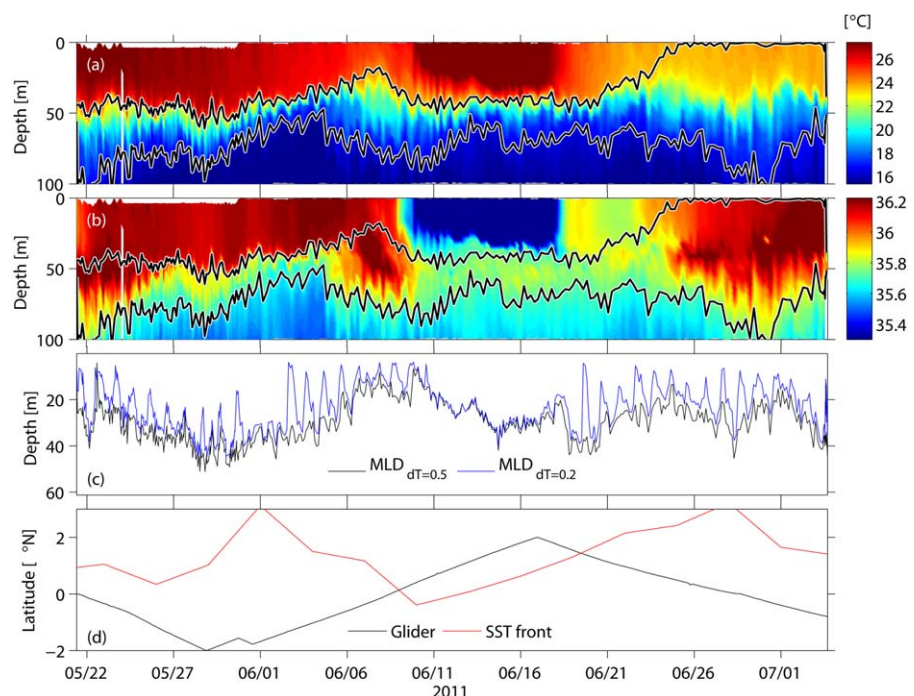

Figure 8. Same as Figure 7, except for glider ifm11 profiling along a meridional section at about 15.5°W.
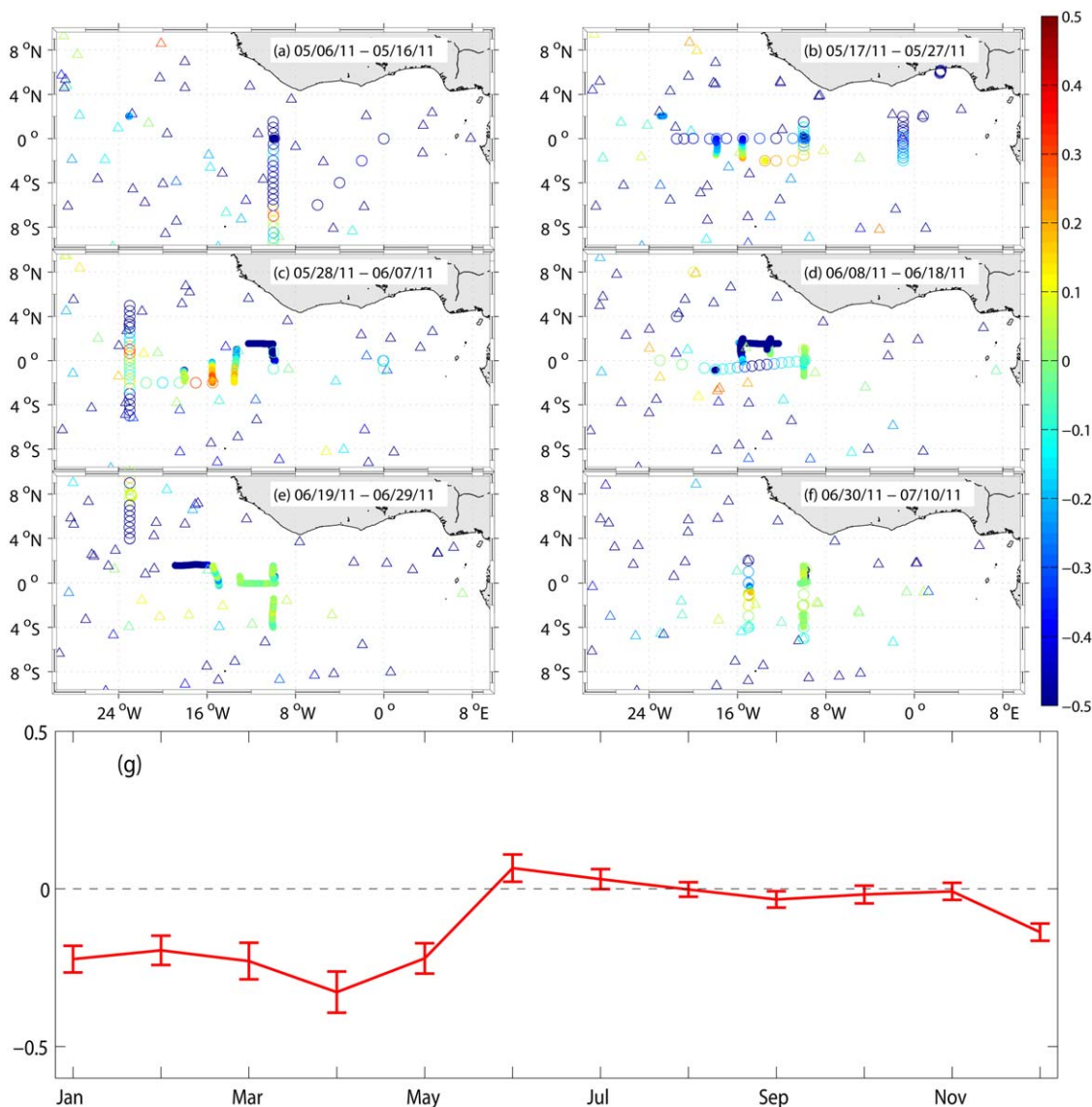
Figure 9. (a–f) Salinity difference between MLS and maximum salinity in the upper thermocline layer below the ML ($24.5 \leq \sigma_\theta \leq 26.2$ or $\sigma_{MLD} \leq \sigma_\theta \leq 26.2$ if $\sigma_{MLD} > 24.5$) from glider profiles (filled circles), shipboard CTD profiles (open circles), and Argo float profiles (triangles) for the CTE. (g) Mean salinity difference between MLS and maximum salinity in the upper thermocline layer ($24.5 \leq \sigma_\theta \leq 26.2$) from all Argo float profiles from the years 2000 to 2012 in boxes with the longitudinal boundaries 23°W and 10°W and the latitudinal boundaries 2°S and 1°N. Red bars denote the standard error of the mean of all profiles in the box within 1 month.

(PIRATA-FR21) and Argo float profiles. The results revealed a general reversal of the upper-ocean vertical salinity gradient (Figure 9). At the beginning of the CTE, the thermocline layer (TL; defined with the potential density range: $24.5 \leq \sigma_\theta \leq 26.2$) was more saline than the ML in the entire equatorial ACT region (Figure 9a). This is due to the fact that the TL contains the EUC core that is advecting high-saline waters from the west during this period. However, south of the equator, the ML was saltier than the TL during May and beginning of June (Figures 9b–9d). This reversed vertical salinity gradient weakened later at the end of June and the beginning of July, when MLS and the TL-salinity became equal in the ACT region (Figures 9e and 9f). Note, that during June and July, the upper boundary of the TL ($\sigma_\theta = 24.5$) reached the sea surface (Figures 7b and 8b). The described variability of the vertical salinity gradient is independent of the measurement device and visible in glider profiles as well as CTD and Argo float profiles. Taking the mean seasonal cycle of the salinity difference between ML and TL from Argo, it is obvious that the difference changes sign in boreal summer (Figure 9g). While the mean seasonal cycle of the difference is a robust feature, its magnitude depends on the latitudinal boundaries used for averaging.
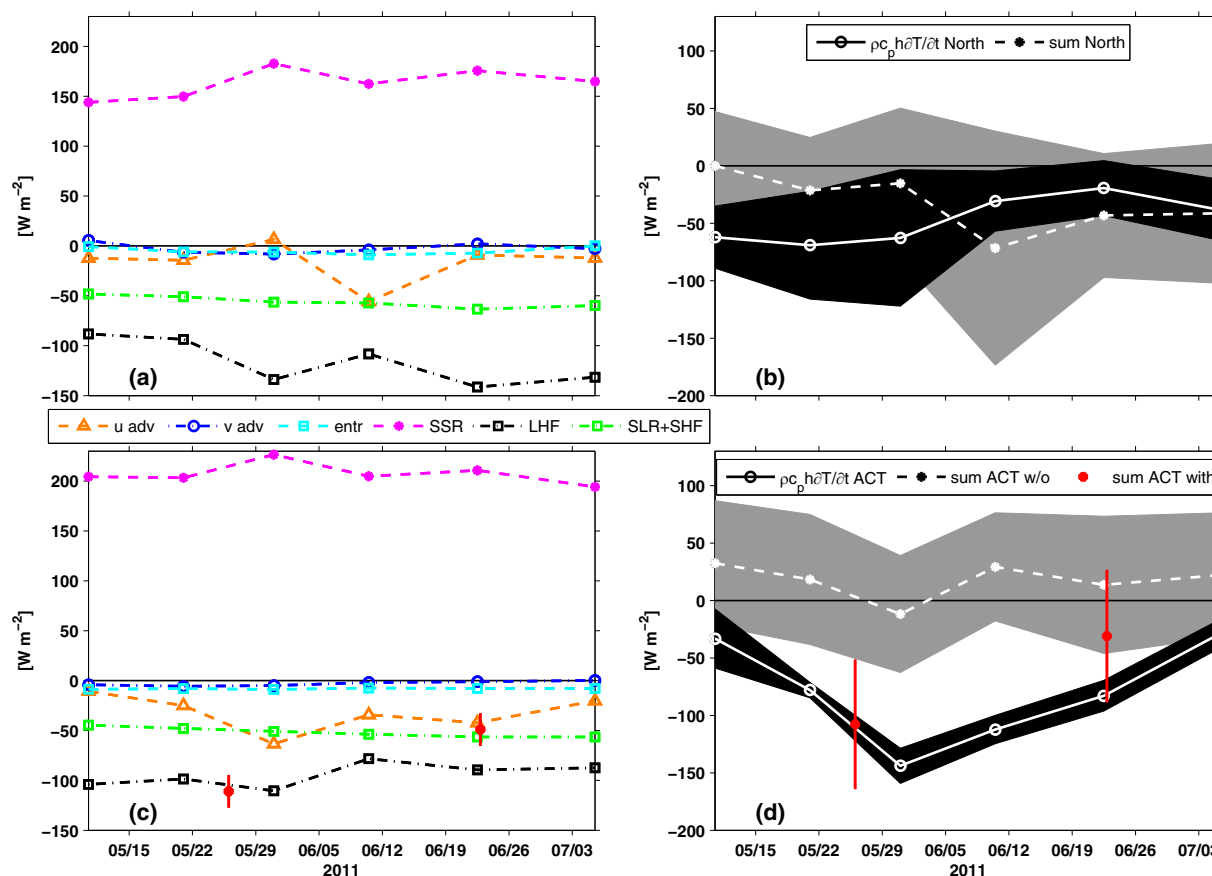
SCHLUNDT ET AL. 7896

Figure 10. (a and c) The contribution of each term to the ML heat budget and (b and d) the local heat tendency and the sum of the terms for the northern box (Figures 10a and 10b) and for the ACT box (Figures 10c and 10d). The different contributions in Figures 10a and 10c are zonal (u adv) and meridional (v adv) heat advection, entrainment (entr), net surface shortwave radiation corrected for the penetrative part (SSR), latent heat flux (LHF), and the sum of net surface longwave radiation (SLR) and sensible heat flux (SHF). The contribution of diapycnal mixing in Figure 10c is shown with the red dots (each dot is representative for the averaging period of about 1 month). In Figure 10d, the sum without (sum ACT w/o; dashed-dotted line) and with (sum ACT with; red dots) diapycnal mixing is shown. The black shadings in Figures 10b and 10d are the uncertainty of the observed heat changes. The grey shadings in Figures 10b and 10d are the accumulation of all errors of the different processes.

3.2. Heat Budget

The contributions of the different processes (equation (1)) to the ML heat budget in the North box (Figures 10a and 10b) and the ACT box (Figures 10 c and 10d) are described in the following. Since this study focuses on the cold tongue development, we start with the ACT box.

3.2.1. ACT Box

Absorbed shortwave radiation in the ACT ranged from 194 ± 36 to 226 ± 36 Wm^{-2}. The variability is caused by the variability of cloud cover and ML thickness. The latent and sensible heat fluxes as well as the net surface longwave radiation cooled the ML throughout the CTE (Figure 10c). The net surface longwave radiation in the ACT box was nearly constant (ranging from 42 ± 10 to 55 ± 10 Wm^{-2}) during the CTE due to the balance of outgoing and downward longwave radiation. Outgoing longwave radiation slightly weakened with decreasing SSTs and the downward longwave radiation weakened with the reduction of clouds. The latent heat flux ranged between a maximum of 110 ± 21 Wm^{-2} and a minimum of 78 ± 21 Wm^{-2}. The variability was predominantly associated with varying winds. The magnitude of the sensible heat flux from the ocean to the atmosphere was the smallest compared to the aforementioned heat fluxes with a mean of 2 ± 3 Wm^{-2}. The resulting net surface heat flux warmed the ML during the whole CTE with a mean of 61 ± 43 Wm^{-2}.

The strong heat loss of the ACT ML in boreal summer can only be explained by ocean dynamics. Zonal heat advection played an important role for ML cooling during the CTE with strongest cooling of -63 ± 25 Wm^{-2} at the end of May, while meridional heat advection was a minor contributor to cooling with a maximum of -5 ± 11 Wm^{-2}. Similar results were obtained for the Mercator assimilation model, where

meridional heat advection showed a maximum contribution of -12 ± 1 Wm^{-2}. Entrainment consistently cooled the ML with a mean -8 ± 1 Wm^{-2} resulting from high vertical velocities in combination with a weak positive vertical temperature gradient below the ML.

In accordance with the reduced SST, the ML heat content tendency in the ACT box was negative during the entire CTE period (Figure 10d). The tendency was weakly negative during early May, but strongly negative during the period end of May to early June, when the ML locally lost up to -144 ± 15 Wm^{-2} of heat. Without considering diapycnal mixing (Figure 10d), the mixed layer heat tendency cannot be explained by the sum of processes described above.

The diapycnal heat flux determined from the microstructure data was elevated during the first period of the CTE from the second half of May to the beginning of June. For this period, a mean flux of -111 ± 16 Wm^{-2} was estimated that reduced in magnitude to -49 ± 9 Wm^{-2} during the second half of the CTE (Figure 10c). Unfortunately, microstructure observations were not continuously available for the entire CTE period within the ACT box thus longer averaging periods had to be used to estimate representative diapycnal heat flux contributions. The elevated diapycnal heat flux during the first period of the CTE resulted from elevated turbulent eddy diffusivities that persisted despite increased upper-ocean stratification during this period.

The magnitude and temporal variability of the sum of the individual heat flux contributions including the diapycnal heat flux (Figure 10d) agrees well with the magnitude and temporal variability of the heat content tendency. This indicates that within the uncertainties, the heat budget in the ACT region was closed utilizing the above flux estimates for the sampled period.

3.2.2. Northern Box
The dominant processes contributing to the heat balance of the northern box differ from those dominating the ACT heat balance. In particular, the net surface heat flux was comparably lower and even changed sign during the CTE. Absorbed shortwave radiation ranged from 144 ± 35 to 183 ± 35 Wm^{-2} and was mainly balanced by the heat loss due to the other atmospheric fluxes (sum ranging from -142 ± 24 to -205 ± 24 Wm^{-2}) (Figure 10a). However, the net surface heat flux warmed the ML in the beginning of the CTE with 8 ± 42 Wm^{-2}, while it cooled the ML during the rest of the experiment with a minimum of -29 ± 42 Wm^{-2} at the end of the CTE. This was mainly caused by the increased cooling contribution of the latent heat flux due to the increased wind.

Zonal heat advection significantly contributed to cooling of the ML only during the beginning of June (-56 ± 68 Wm^{-2}), but was small during the rest of the CTE period. The contribution of meridional heat advection to ML cooling in the northern box was in general small with a minimum value of -8 ± 49 Wm^{-2}. The high uncertainties for the advection terms result, on the one hand, from the uncertainties in velocity, estimated through comparison of OSCAR velocities with velocities from moored measurements and, on the other hand, from uncertainties of estimating the horizontal temperature gradients from the satellite data. The contribution of entrainment ranged from -1 ± 2 to -9 ± 2 Wm^{-2} during the whole CTE and is not important for ML cooling. The diapycnal heat flux was not estimated for the northern box due to the lack of data.

The ML heat content tendency was negative throughout the CTE (Figure 10b). The negative tendency was largest at the end of May/beginning of June (-70 ± 47 Wm^{-2}) while it was smallest (-19 ± 24 Wm^{-2}) at the end of June. During the whole CTE period and within the given uncertainties, the sum of the aforementioned individual flux terms balances the ML heat content tendency.

3.3. Salinity Budget
The contributions of the different processes (equation (2)) to the MLS budget in the North box (Figures 11a and 11b) and in the ACT box (Figures 11c and 11d) are described in the following. As for the heat budget, we start with the ACT box.

3.3.1. ACT Box
Evaporation in the ACT region increased MLS constantly at a rate between 0.16 ± 0.03 and 0.20 ± 0.05 per month (month^{-1}), while precipitation reduced the MLS only weakly in the beginning of May (Figure 11c). The contribution of precipitation to MLS changes during the development of the ACT was negligible, due to the position of the ITCZ further to the north (Figure 11c). Hence, the difference E-P is at this location dominated by evaporation.
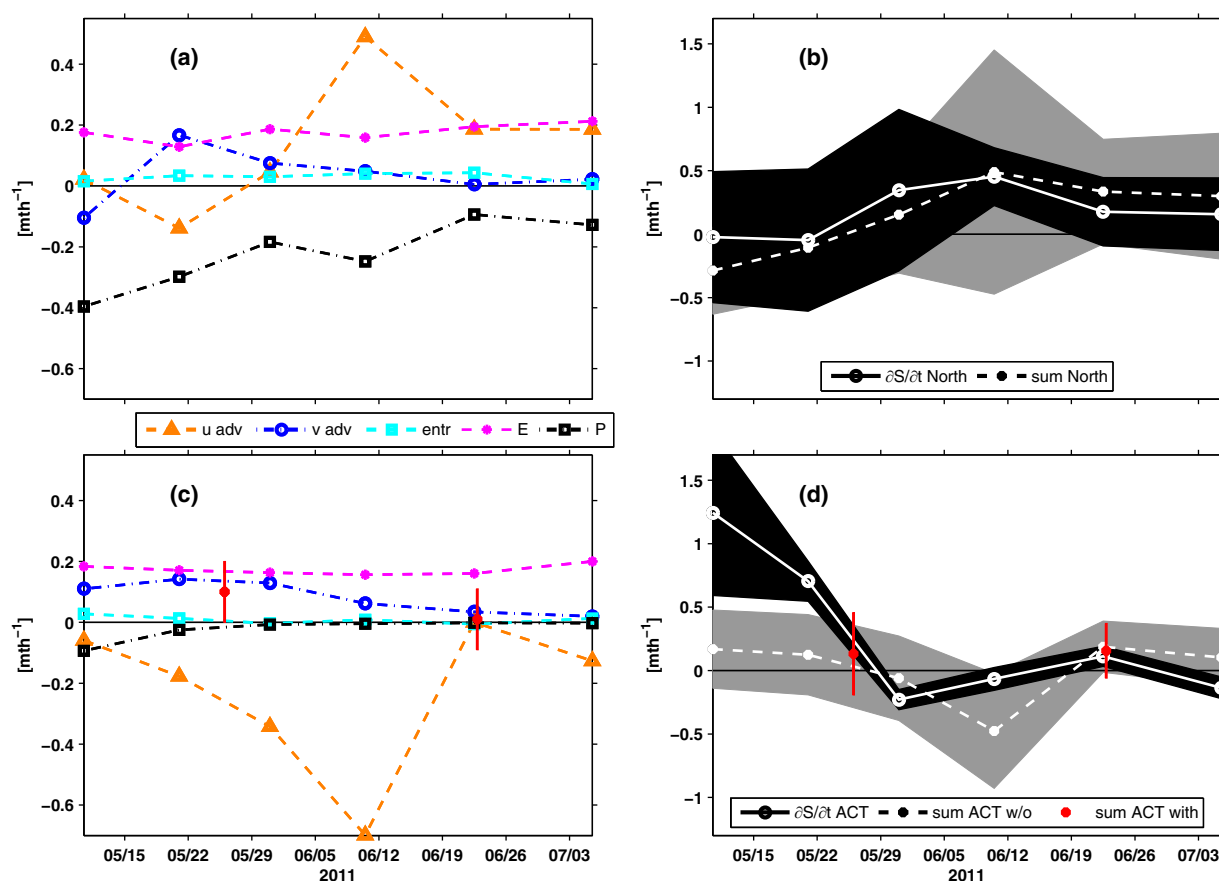
Figure 11. (a and c) The contribution of each term to the MLS budget and (b and d) the local salinity tendency and the sum of the terms for the northern box (Figures 11a and 11b) and for the ACT box (Figures 11c and 11d). The different contributions in Figures 11a and 11c are zonal (u adv) and meridional (v adv) salinity advection, entrainment (entr), evaporation (E), and precipitation (P). The contribution of diapycnal mixing in Figure 11c is shown with the red dots (each dot is representative for the averaging period of about 1 month). In Figure 11d, the sum without (sum ACT w/o; dashed-dotted line) and with (sum ACT with; red dots) diapycnal mixing is shown. The black shadings in Figures 11b and 11d are the uncertainty of the observed salinity changes and the gray shadings in Figures 11b and 11d are the accumulation of all errors of the different processes.

By far, the largest absolute contribution to the MLS budget was by zonal advection. In May and the beginning of June 2011, negative salinity anomalies were transported into the ACT within the westward branches of the SEC. Minimum salinity advection occurred in early June contributing to a freshening of -0.70 ± 0.37 month^{-1}. However, zonal advection exhibited elevated variability throughout the CTE and almost disappeared in the middle of June when it contributed to a weak salinity increase of 0.01 ± 0.01 month^{-1}.

Meridional salinity advection increased MLS in May and the beginning of June 2011 with a maximum contribution of 0.11 ± 0.20 month^{-1} (Figure 11c). During the rest of the CTE, the contribution of meridional advection was weak. Entrainment also played a minor role for salinity changes in the ML during the CTE with a maximum value of 0.03 ± 0.01 month^{-1}. As vertical velocities used for the entrainment estimates in the salinity and the heat budgets are the same, the minor role of entrainment in the salinity budget is due to the small vertical salinity gradients below the ML as pointed out in section 3.1.

The diapycnal salt flux inferred from microstructure observations increased MLS by 0.10 ± 0.01 month^{-1} during the first period of the CTE (Figure 11c). It decreased in June and locally partly changed sign in the end of June/beginning of July around 10°W, according to a local change in sign of the vertical salinity gradient (Figure 7b). However, the average diapycnal salt flux determined from all data collected between the second week of June and the end of the CTE resulted in a very weak salt flux of 0.01 ± 0.01 month^{-1} (Figure 11c).

The MLS in the ACT box increased with the cold tongue onset in May 2011, with a maximum tendency of 1.24 ± 0.65 month^{-1} (Figure 11d). This tendency reduced during the further expansion of the cold tongue and was followed by a period of weak ML freshening. With the data sets available for this study, the salinity content change during cold tongue development could not be fully balanced by the individual flux

contributions, although contributions due to diapycnal mixing were evaluated here. The latter accounted for some of the salinity content increase observed during the beginning of the experiment, but an unresolved residual remained.

3.3.2. Northern Box

Evaporation in the northern box was similar to the evaporation in the ACT box and weakly increasing during the CTE from 0.13 ± 0.03 to 0.21 ± 0.06 month^{-1}. In analogy to the latent heat flux, this increase was caused by the increasing wind speed. The main source of freshwater in the northern box during the CTE was precipitation (Figure 11a). The ITCZ occupied parts of the northern box during the CTE, which led to an elevated freshwater input of predominantly convective rainfall resulting in a maximum salinity decrease of -0.40 ± 0.11 month^{-1} at the beginning of May. Hence, the difference E-P was negative during most parts of the CTE and only changed sign in the second half of June.

Similar to the ACT box, zonal advection played a key role in salinity changes for the northern box (Figure 11a). During May, westward flow transported negative salinity anomalies into the northern box from the east leading to a minimum of zonal salinity advection of -0.14 ± 0.12 month^{-1}. Later in June, elevated zonal salinity advection of up to 0.49 ± 0.6 month^{-1} contributed to increase MLS. This is caused by positive salinity advection with the nSEC, which was strong during June. However, this contribution is uncertain due to the misrepresentation of TIWs in the OSCAR product.

Meridional salinity advection contributed to increase MLS during May and June except at the beginning of the CTE in early May. Northward flow transported salty water from the cold tongue into the northern box with a maximum contribution of 0.17 ± 0.35 month^{-1}. Entrainment derived from model output was weak during the CTE with a maximum contribution of 0.04 ± 0.01 month^{-1} in mid-June. The diapycnal salt flux was not estimated for the northern box due to the lack of data.

In the northern box, MLS tendency was positive during the whole CTE except for a weak freshening during the beginning of the experiment (Figure 11b). The MLS tendency was balanced within the uncertainties by the sum of precipitation, evaporation, horizontal advection, and entrainment during most of the CTE period.

3.4. The CTE in the Seasonal Cycle

In order to incorporate the different contributions to the ML budgets inferred during the CTE into a broader perspective, we compare the results obtained for the period of the CTE to the mean seasonal cycle of the contributions to the ML budgets estimated at three PIRATA buoy locations within our study area. For the salinity budget, the seasonal cycles of the individual contributions are estimated in the following at the three PIRATA buoy sites at 23°W and 10°W on the equator, as well as 4°N, 23°W (Figure 12). The seasonal ML heat budgets at these locations were already examined in various previous studies [*Foltz et al.*, 2013, 2003; *Hummels et al.*, 2013]. Hence, the results of the CTE concerning the ML heat budgets are compared to the results of these previous studies as part of section 4.

3.4.1. Mean Seasonal Mixed Layer Salinity Budgets
3.4.1.1. 4°N, 23°W

The variability of precipitation dictates the mean seasonal cycle of MLS tendency at the PIRATA buoy site at 4°N, 23°W. It follows a semiannual cycle caused by the seasonal migration of the ITCZ (Figure 12a). During May-July, the contribution weakens due to the northward migration of the ITCZ. However, although it is reduced during this period, precipitation was the dominant contributor to MLS changes in the northern box during the CTE (Figure 11a). Monthly mean evaporation is nearly constant over the year, but reduced compared to evaporation at the two equatorial locations. Hence, the net surface freshwater flux at 4°N, 23°W is predominantly determined by the semiannual cycle of precipitation and is only positive in July and August, when precipitation is strongly reduced.

The seasonal cycle of zonal advection at the buoy site is weak and follows the seasonal cycle of the NECC, which strengthens from its minimum eastward velocity during boreal spring to maximum eastward velocities in July [e.g., *Richardson and Reverdin*, 1987; *Goes et al.*, 2013]. The monthly mean zonal advection during May-July at the buoy site is much weaker than suggested for the northern box during the CTE period in 2011. In particular, the variability of zonal advection included a change in sign during the CTE, which is not captured in the seasonal estimate at the buoy location.
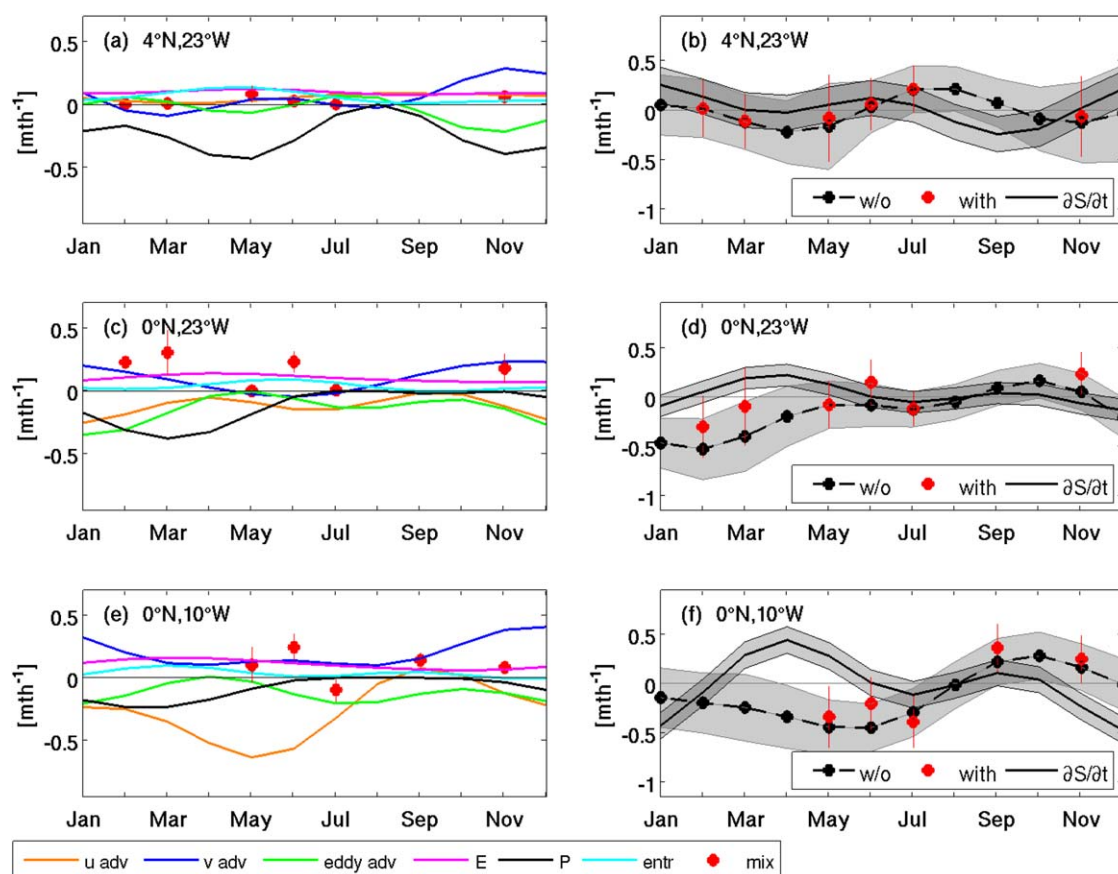
Figure 12. (a, c, and e) Seasonal cycles of the contributing terms to the MLS budget and (b, d, and f) the comparison of the local salinity tendency and the sum of the contributing terms at three PIRATA buoys. The different contributions in Figures 12a, 12c, and 12e are zonal (u adv), meridional (v adv), and eddy (eddy adv) salinity advection, evaporation (E), precipitation (P), entrainment (entr), and diapycnal mixing (mix). Black dashed-dotted lines (right) are the sum without diapycnal mixing and red dots are the sum with diapycnal mixing. The gray shadings in Figures 12b, 12d, and 12f are the accumulation of all errors of the different processes and the error of the salinity tendency.

Meridional advection has its maximum in late fall/early winter and is the main contributor for the increase of the MLS this period (Figure 12a). Eddy salinity advection exhibits a weak semiannual cycle with a freshening contribution in April/May and from October to December. During the latter period, eddy salinity advection is elevated but negative, leading to a decrease of MLS content. The sum of the seasonal cycle of meridional salinity advection and eddy salinity advection, dominated by the meridional eddy advection due to the TIWs, at the mooring site is small in boreal summer, which is similar to the total meridional salinity advection estimated during the CTE. The sum during May is negative, indicating negative total meridional salinity advection, which was not determined from the data collected during the CTE period. During June and July, the sum is positive, indicating a total meridional salinity advection similar to the results obtained for the same period of the CTE.

Entrainment is weak throughout the year and exhibits a maximum in spring. During the CTE, the entrainment in the northern box was similarly weak. The diapycnal salt flux is negligible throughout the year, at least during the resolved periods. The sum of the contributing terms balances the observed salinity tendency within the uncertainties over the entire year at the PIRATA buoy at 4°N, 23°W (Figure 12b). Although the seasonal cycle was evaluated locally, the results generally agree with the findings during the CTE pointing toward the fact that the salinity variability observed during the CTE is typical for this season (Figures 11b and 12b).

3.4.1.2. 0°N, 23°W
From January to May, precipitation exceeds evaporation at the equatorial PIRATA buoy at 23°W representing the western ACT region (Figure 12c). Later in the year, precipitation is negligible and nearly constant evaporation yields a positive surface freshwater flux during that part of the year. Similarly, in 2011 during

the CTE period from May to July, the influence of precipitation on the MLS budget was weak in the ACT region and a positive freshwater flux due to excess evaporation with only weak variability was indicated. This freshwater flux contributed to a MLS increase, comparable to the climatological freshwater flux from May to July (Figure 12c).

The zonal salinity advection at the buoy site is negative throughout the year representing a significant contribution to the total salinity budget. It is characterized by a weak semiannual cycle that peaks in boreal summer and winter. The negative salinity advection during early boreal summer is consistent with the results from the CTE period, but weaker in magnitude. Meridional salinity advection exhibits a maximum in boreal winter and represents the largest positive flux contribution to the MLS budget. Eddy salinity advection reduces MLS content at 23°W and is largest in the boreal winter months. At the end of spring, the contribution is negligible but is again relevant during summer. The sum of the seasonal cycle of mean meridional advection and eddy salinity advection at the buoy site is small in boreal summer. Due to the fact that eddy variability at 23°W is dominated by TIWs and the meridional gradients exceed the zonal ones, eddy advection is presumed to consist mostly of the meridional eddy component. The small magnitude of the total meridional heat advection agrees with the results from the CTE (Figure 12c), however, the sign differs to the CTE results, where weak positive meridional heat advection is found.

Within the seasonal cycle, entrainment at the PIRATA buoy at 23°W has its maximum during May and June (Figure 12c) when it contributes to a salinity increase. During the rest of the year, its contribution is weak. Within the ACT and during the CTE period in 2011, the weak salinity difference between the ML and below the ML resulted in weak entrainment contributions to MLS changes, albeit elevated entrainment velocities.

The diapycnal salt flux calculated from individual cruise data (section 2.5.3) exhibits elevated variability within the seasonal cycle at 23°W. Strongest diapycnal salt flux, leading to a MLS increase occur during February-March. Additionally, diapycnal salt fluxes are elevated in June and November. In May and July, its contribution at 23°W is weak. The results for June and July are comparable to the CTE results from 2011, when the diapycnal salt flux led to a MLS increase in June and had a negligible contribution in July.

The seasonal cycle of the salinity tendency at the equatorial PIRATA buoy at 23°W is weak, but shows a positive tendency during spring, which reduces and even reverses toward July (Figure 12d). The weak variability of the MLS tendency is generally captured by the sum of the contributing terms. In February and March, the salinity-increasing contribution of diapycnal mixing decreases the imbalance between tendency and the sum of fluxes. During this period, large freshening contributions result from zonal advection, eddy advection as well as precipitation while the diapycnal flux increases MLS together with meridional advection and evaporation. Although the seasonal cycle was evaluated locally, the results generally agree with the findings during the CTE pointing toward the fact that the salinity variability observed during the CTE is typical for this season (Figures 11d and 12d). However, some flux contributions may vary locally within the ACT during the seasonal cycle.

3.4.1.3. 0°N, 10°W

In winter and early spring, the mean seasonal cycles of evaporation and precipitation at the equatorial PIRATA buoy site at 10°W are comparable in magnitude, resulting in a weak surface freshwater flux (Figure 12e). During the rest of the year, evaporation exceeds precipitation, thus the surface freshwater flux contributes to increase MLS. This is comparable to the freshwater flux in the ACT region during the CTE period. Additionally, comparable results of the surface freshwater flux were obtained by *Da-Allada et al.* [2013] for the GG, suggesting that the surface freshwater flux is a large-scale phenomenon during this period.

Zonal advection is the largest contributing term to the mean seasonal cycle of the MLS balance at the equator at 10°W. It acts to reduce MLS and is most pronounced from December to July. Later in the year, its contribution weakens (Figure 12e). Although zonal advection at 23°W is reduced compared to 10°W, zonal advection in the ACT region during the CTE period is of similar magnitude compared to 10°W and also shows a similar temporal evolution. This freshening contribution to the MLS balance can be explained by negative salinity advection mainly associated with the westward current branches, the northern SEC (nSEC), and the central SEC (cSEC). However, as will be discussed in section 4, the seasonal evolution of zonal salinity advection is predominantly controlled by the seasonal evolution of zonal MLS gradients. In general, the spring/early summer dominance of zonal advection in the MLS budget found here also agrees with recent results from a model study of the MLS balance in the GG region reported by *Da-Allada et al.* [2013].

Similar to the results from 23°W, the contribution of meridional advection to the MLS budget has a maximum in late fall/early winter. During this period, the meridional salinity advection represents the dominant MLS source at 10°W (Figure 12e). Magnitude and phase of eddy salinity advection at 10°W is also very similar to 23°W. It exhibits a semiannual cycle with minimum in December/January and July/August. The sum of the seasonal cycle of meridional salinity advection and eddy salinity advection at the buoy site is again small (cf. 23°W) in boreal summer, which is similar to the total meridional salinity advection estimated during the CTE. Also as for 23°W, the sum during June and July is negative, indicating freshening due to meridional salinity advection, which was not found during the CTE.

The seasonal cycle of entrainment at the PIRATA buoy at 10°W has its maximum in March and April contributing to the MLS increase during this period (Figure 12e). During the rest of the year, the contribution of entrainment is weak. This is consistent with the estimate of entrainment during the CTE, when the contribution of entrainment was rather negligible due to weak salinity differences between the ML and below the ML albeit rather strong entrainment velocities. Weak positive and negative entrainment contributions to MLS changes were obtained due to changes in sign of the vertical salinity gradient below the ML.

The diapycnal salt flux at the 10°W-PIRATA buoy increases the MLS in May and June, followed by a freshening contribution during July. Later in September and November, again a positive salt flux from the subsurface layer into the ML through diapycnal mixing was observed. The findings for June and July are comparable with the CTE results that showed a positive diapycnal salt flux, leading to a MLS increase during June, followed by a negligible contribution to the MLS budget in July 2011.

The observed MLS increase during May 2011 in the ACT region is identifiable in the seasonal cycle of the salinity tendency at 10°W (and 23°W) as well (Figure 12f). This increase weakens during June and July in the central ACT region. The MLS increase at the equatorial PIRATA buoy site at 10°W is not explained by the considered processes from equation (2). The remaining residual indicates either a missing source of salinity or an overestimate of the freshening contributions (Figure 12f). Observed diapycnal mixing in May and June provides a positive salt flux into the ML and thus reduces the residual, leading to a balanced salinity budget within the uncertainties at least during June. From March to May, vertical salinity gradients between the ML and the thermocline are largest (cf. Figure 9). It is thus likely that diapycnal mixing during this period contributes to increase MLS and thus decrease the residual. However, so far no microstructure observations from 10°W during these months are available. The remaining imbalance between the sum of terms and the observed salinity tendency at this location also coincides with periods of highly elevated zonal advection (March to July) and periods of elevated meridional advection (September to December). Possibly, the remaining imbalance is caused by an overestimation of these terms, which is either caused by overestimated horizontal velocities or horizontal salinity gradients. As the same velocity product did not cause imbalances in the ML heat budget at this location in another study [*Hummels et al.*, 2014], it could be argued that the zonal and meridional salinity gradients are still not sufficiently well resolved by Argo floats.

4. Summary and Conclusion

Within the present study, the physical processes responsible for MLT and MLS changes during cold tongue development in 2011 have been investigated using an extensive set of in situ and satellite data, reanalysis products, and assimilation model output. In contrast to other studies evaluating the ML heat and salinity budget at individual locations or empirically defined boxes, the strategy pursued here was to evaluate the individual contributions to the ML budgets in two boxes representing the western ACT region and a region to the north of it. The boundary between the two boxes was defined by the temporally varying maximum of the meridional SST gradient. In general, the results concerning the ML heat budget agree with previous studies of the same region [*Hummels et al.*, 2013; *Jouanno et al.*, 2011a; *Wade et al.*, 2011], despite the different approaches regarding box-averaged or local budgets. The diapycnal heat flux stands out as the dominant cooling term during ACT development, which has been inferred here from microstructure observations distributed within the ACT box. This finding is in agreement with previous studies [*Hummels et al.*, 2013; *Jouanno et al.*, 2011a]. It also gives confidence that the chosen region for averaging is adequate to investigate the contributions to the ML budgets representative for the western ACT.

The MLS budget has to our knowledge not been investigated within this region before. MLS tendency is positive during ACT development. However, diapycnal mixing played only a minor role in the MLS budget. This is

due to a rather weak vertical salinity gradient in the western ACT during the period of the CTE, which partly even changed sign. The horizontal salinity advection, especially its zonal component, represents the dominant contribution to the MLS budget. Contrary to the MLT budget, the MLS budget is partly not closed within the estimated uncertainties, although considering diapycnal flux contributions. This suggests the presence of unaccounted errors in the MLS budget that might result from the used products or methodology. In summary, tendencies and major flux contributions to MLT and MLS within the CTE period from May to July 2011 were:

ACT box

1. The heat content tendency of the ML was negative throughout the CTE period. The net surface heat flux constantly warmed the ML. Dominant cooling terms were diapycnal mixing through the ML base and zonal advection associated with the transport of cold water from the GG. The sum of these contributions balanced the observed MLT changes within the uncertainties.
2. MLS tendency was positive at the beginning of the CTE in May and became close to zero in June and July. Evaporation exceeded precipitation throughout the CTE. Horizontal salinity advection was the dominant contributor to ML freshening from May to mid-June. Entrainment was negligible throughout the CTE. The contribution of diapycnal mixing was relatively small. The sum of these contributions balanced the observed MLS changes within the uncertainties in June and the beginning of July. A residual between observed MLS changes and the sum of all contributions remained during May.

Northern box

1. Heat content tendency was negative during the CTE but considerably lower when compared to the ACT box. Net surface heat flux was small, warming the ML at the beginning of the CTE and cooling the ML afterward. Horizontal heat advection cooled the ML during the entire CTE, except at the end of June, when advection weakly warmed the ML. Entrainment weakly cooled the ML throughout the CTE. The sum of these contributions balanced the observed MLT changes within the uncertainties.
2. The MLS decreased during May and increased later in June and July. Precipitation was the main contributor to MLS changes during the beginning of the CTE in May, when zonal and meridional advection cancelled out each other. In June and July, when precipitation and evaporation were of similar magnitude, horizontal salinity advection, mainly the zonal component, was the main contributor to the MLS increase, particularly in the beginning of June. The observed MLS tendency was balanced within the uncertainties by the sum of resolved flux contributions.

To address the generality of the results obtained during the period of the CTE, the mean seasonal cycle of the contributions to the MLS budget was evaluated at three PIRATA buoy locations, on the equator at 23°W and 10°W and at 4°N, 23°W. Overall, the dominant flux contributions determined at the buoy positions for the CTE period agreed well in magnitude and phase with the box averaged flux contributions. At the equatorial buoy site at 10°W, zonal salinity advection is the dominant term contributing to a freshening of the ML from December to July (Figure 12e) and the magnitude of the contribution is a factor of two larger in the central ACT region at 10°W compared to the western ACT region at 23°W (Figure 12c). Precipitation and meridional eddy advection also significantly contribute to a freshening of the ML within the ACT region throughout the year. Meridional advection, entrainment, and evaporation contribute to increase MLS. Finally, diapycnal mixing increases salinity predominantly from November to June and is negligible during the other months of the year. The results emphasize that the MLS tendency is largely balanced by ocean processes and to a lesser extent by the net surface freshwater flux (see Figure 12).

Furthermore, the evaluation of the mean seasonal cycles at the PIRATA buoy locations emphasized that zonal salinity advection is the main contributor to the MLS budget in the western ACT during the first half of the year. Two major branches of the SEC, the nSEC slightly north of the equator (mean position: ~1°N at 10°W and ~2°N at 23°W) and the cSEC south of the equator (mean position: ~3°S–4°S at 10°W and ~4°S at 23°W) [e.g., *Lumpkin and Garzoli*, 2005; *Brandt et al.*, 2006; *Kolodziejczyk et al.*, 2009], provide negative salinity advection. However, its contribution rapidly weakens toward the end of June. Due to the fact that the two branches of the SEC are still present during this period, the strong weakening of zonal salinity advection results from a decrease of the zonal salinity gradient. In fact, a large MLS increase in the EEA in

June and July 2011 was observed in the SMOS SSS (Figure 6). As evaporation increases MLS in the central and EEA homogeneously, the elevated MLS in the EEA must have their origin in subsurface processes. Recently, *Kolodziejczyk et al*. [2014] conjectured vertical diffusion toward the sea surface in the GG occurring between May and August as the fate of the high-saline thermocline waters that are transported eastward within the EUC during the spring period [*Johns et al*., 2014]. This requires enhanced diapycnal mixing in the GG from late boreal spring through summer, which was indeed indicated by numerical simulations with a general circulation model [*Jouanno et al*., 2011b].

Although the salinity flux into the ML associated with diapycnal mixing was weak during the CTE, it is in general a salinity-increasing contributor to the MLS budget of the ACT. This is due to the fact that the EUC core is generally associated with a subsurface salinity maximum and hence diapycnal mixing acts to increase MLS. Surprisingly though on some stations in the central ACT region, diapycnal mixing partly contributed to decrease MLS in boreal summer. These local freshening events are due to the local reversal of the vertical salinity gradient below the ML. The question arises which processes are responsible for the reversal of the vertical salinity gradient. According to the findings of *Jouanno et al*. [2011b] and as hypothesized in recent studies by *Kolodziejczyk et al*. [2014] and *Johns et al*. [2014], a possible explanation is that a part of the additional salt in the ML was previously entrained or mixed from the thermocline layer in the GG (and parts of the central ACT) upward, simultaneously eroding the salinity maximum of the EUC. Evaporation further increased the MLS, finally leading to a strong reduction or reversal of the vertical salinity gradient below the ML. Differing meridional displacements of existing meridional salinity gradients in the ML and the EUC below due to TIWs might as well contribute to local changes in the vertical salinity gradient below the ML, which is illustrated by the glider section at the PIRATA buoy at the equator, 10°W.

Strong local differences of vertical gradients and diapycnal diffusivities at the base of the ML within the ACT box were observed. Diapycnal fluxes calculated by using box averages of vertical gradients and diapycnal diffusivities do not agree with the box average of locally calculated diapycnal fluxes due to a correlation of vertical gradients and diapycnal diffusivities. Similarly, diapycnal mixing as conjectured from box-averaged budget residuals might become erroneous when averaging over larger regions. Microstructure observations as they are used here are still rather sparse. To get more reliable estimates on the variability in space and time of the diapycnal heat and salt fluxes at the ML base, other observational platforms have to be used with higher spatial and/or temporal resolution such as, e.g., gliders equipped with microstructure sensors or moored microstructure measurements.

For the calculation of the horizontal advection, surface or upper-ocean currents are necessary together with horizontal gradients of MLT and MLS. To estimate box averages of the advection, a velocity product is needed with a high temporal and spatial resolution within the entire box. In this study, the OSCAR product is used, which is estimated from satellite observation and not directly constrained by observations. In particular, in the equatorial band, OSCAR velocities strongly deviate from subsurface ADCP velocities measured at PIRATA locations (Figure 4) and also from velocities of the MERCATOR assimilation model. The discrepancy in the velocity products results in a large uncertainty of the box-averaged horizontal advection for the CTE.

A general good agreement between in situ SSS and SMOS SSS was shown for the cold tongue region with an estimated accuracy of satellite SSS similar to the previous studies [*Boutin et al*., 2013, 2012; *Reul et al*., 2012]. In regions strongly affected by precipitation, substantial differences between SSS and MLS were observed (Figure 3) that introduce additional uncertainty when using SSS for studying ML processes. However, the steadily improving SSS measurements are the basis for improving the MLS budget particularly by better constraining individual contributions due to the different atmospheric and oceanic processes in dynamically varying regions.

Together with several previous studies, the present study improved our understanding of the seasonal and intraseasonal variability of temperature and salinity within the ML in the central equatorial Atlantic. The interesting question regarding the contribution of different processes to interannual variations of ML properties and thus to a deterministic or stochastic behavior of climate relevant SST variability remains to be addressed in future studies.

Appendix A: Box Clustering of the Data

Time series of glider observations were used to study the upper-ocean variability. The high resolution in time (one profile in approximately 4 h) as well as in space (one profile every 3–4 km) made it possible to

examine the spatiotemporal variability in the central tropical Atlantic. To discriminate between the ACT and the region north of it, two boxes were chosen in which data were averaged. The two boxes are the ACT box characterized by strong cooling and the northern box north of the ACT box with weak cooling during cold tongue development.

Here we used the meridional SST gradient to determine the northern and southern boundary of the ACT box. The maximum SST gradient between 1°S and 4°N defines the northern boundary and the minimum SST gradient between 5°S and 2°S the southern boundary of the ACT box. These boundaries vary in time. A wave-like structure, associated with TIW propagation is weak in May and at the beginning of June in the SST data. In addition, the undulations of the SST front increased in amplitude with the intensification of the cooling. The calculation of the meridional boundaries of the ACT box was done separately with the satellite SSTs and with the model SSTs, due to the different phases of TIW propagation in both products as visible in the meridional velocities at two PIRATA buoy sites (Figure 4c). The zonal boundaries of the ACT box were fixed and set to 23°W and 10°W. The northern box has a fixed northern boundary at 8°N, a western boundary at 23°W and a northeastern boundary connecting 16°W, 8°N with 10°W, 2°N.

The time period of 10 days that was used for averaging all data in the boxes follows from the decorrelation time scales for tropical Atlantic currents. Decorrelation time scale for the meridional currents is between 7–10 days [*Perez et al.*, 2014] and about 8–10 days for the zonal currents [*Garraffo et al.*, 2001; *Lumpkin et al.*, 2002]. The 10 day period is also consistent with the Argo period and the representation of the OSCAR product [*Johnson et al.*, 2007]. The profiles in both boxes were averaged by bootstrapping with 1000 realizations. The mean of all realizations was taken as the value for the box (for MLT, MLS, MLD, the temperature difference between MLT and the temperature below the ML base, the salinity difference of MLS and salinity below the ML base). The error was computed as two standard deviations encompassing ∼95% of the data. Uncertainties for dissipation rates of TKE were estimated by bootstrapping and the propagation of errors was calculated with the procedure of *Ferrari and Polzin* [2005] for diapycnal diffusivities and accordingly for the heat and salt fluxes [*Schafstall et al.*, 2010].

Box-averaged lateral gradients of MLT and MLS were calculated by using satellite SSTs and SSSs. These gridded products are available at 3 day time resolution. Precipitation, evaporation, net shortwave and longwave radiation, as well as turbulent heat fluxes (latent and sensible) through the ocean's surface were averaged over the two boxes. The uncertainty of the box average was determined by taking the error, determined by the comparison with shipboard measurements, at every grid point into account. Errors for the velocities were estimated by comparing satellite-derived velocities with in situ measurements.

Appendix B: Comparison of Atmospheric Data Sets for Heat and Freshwater Fluxes With Observations

For the calculation of the surface radiative and turbulent heat fluxes and the freshwater flux, several products were compared with in situ shipboard measurements, which are a combination of onboard radiation and rain measurement devices, a pyranometer/pyrgeometer system, and an optical disdrometer. The methodology used to compare in situ data and satellite-derived precipitation is described by *Bumke et al.* [2012] for the Baltic Sea and adapted here for the equatorial Atlantic. Due to the high spatial and temporal variability of precipitation, a specific statistical analysis was used that compared in situ precipitation measurements and satellite-derived data or reanalysis data. This analysis follows the recommendations given by the World Meteorological Organization (WMO) for binary or dichotomous forecasts (a detailed description is provided through the "WWRP/WGNE Joint Working Group on Forecast Verification Research" and online available at: http://www.cawcr.gov.au/projects/verification/#Methods_for_dichotomous_forecasts). For comparison, we used hourly data. These 1 h averages of measured rain rates were compared to hourly interpolated fields. We allowed 65 km distance between ship and grid point for AMSR-E, TMI, and SSMIS. For ERA-Interim, we used 120 km and for NCEP2, 240 km according to the data sets spatial resolution. The bias score close to 1 for AMSR-E and SSMIS indicates similar rain probabilities as observed, while rain probabilities for NCEP2 are more than four times and that of ERA-Interim 14 times higher than observed. For TMI data, we estimated a bias score of 0.7. The statistical analysis suggests that we have to take into account that precipitation is a rare event. In this case, an estimate of the performance is the so-called threat score or critical success index (CSI) instead of the correct proportion. The CSI is about 0.3 for the AMSR-E and SSMIS data compared to less

than 0.15 for NCEP2, ERA-Interim, and TMI. These results indicate that SSMIS and AMSR-E data give the most reliable information about precipitation. This is supported by biases in average rain rates, which are of the order of −15% to+30% for SSMIS and AMSR-E, −70% for TMI, +110% for NCEP2, and even +250% for ERA-Interim.

We computed daily mean heat fluxes and evaporation along the cruise track of the research vessel using meteorological data for the estimation of the turbulent heat fluxes and evaporation and the bulk transfer coefficients of *Bumke et al.* [2014]. They estimated the coefficients after the inertial dissipation method and compared their calculated fluxes with fluxes determined after the COARE algorithm [*Fairall et al.*, 2003]. All considered atmospheric products were interpolated on a regular 1° × 1° grid and averaged over 24 h. The grid boxes on the 1° × 1° grid covered by the vessel on 1 day were then averaged. The comparison of the statistical parameters (bias, standard deviation, and rms difference) of the several products against the in situ shipboard measurements (Table 1) indicate larger than observed latent heat fluxes into the atmosphere in the equatorial regions in the reanalysis products. This bias was also found in a validation study of *Kubota et al.* [2003].

The heat fluxes and the evaporation from TropFlux and the precipitation from AMSR-E were chosen for further calculations within this study.

Appendix C: Comparison of Satellite SST and SSS With Observations

All available surface data from glider, float, and CTD measurements as well as hourly averaged thermosalinograph observations were used to compare in situ and satellite data for the period from 7 May to 11 July 2011 (Figure 3). The maximum distance between the closest satellite grid point, from 3 day mean SST and SSS satellite images, and in situ measurements is ~1/6° or ~10 nm. Satellite and in situ SST data agree well (Figure 3a) with a correlation coefficient of 0.98. We estimated (and corrected for the analysis) an offset of −0.17°C ($SST_{TMI} - SST_{in\ situ}$) with a standard deviation of 0.52°C. As expected for the SSS (Figure 3b), the correlation was lower, with a correlation coefficient of about 0.77. The local nature of freshwater anomalies, due to the lack of an air/sea feedback, is expected to be one reason, but also the differences in the observed ocean volume contribute. For example, the dispersion of a freshwater anomaly due to a local rainfall event will be very much confined to the upper few centimeters of the water column and may not be recognized in the near-surface in situ data typically taken below 1 m depth [see also, e.g., *Boutin et al.*, 2013]. This can be evidenced when evaluating SMOS SSS observations coinciding (within 3 day averages) with precipitation events (rain rate $\geq$ 0.1 mm h^{-1}) as observed by AMSR-E. These data points indicate a mean bias of MLS compared to satellite SSS of −0.39 ($SSS_{SMOS} - SSS_{in\ situ}$). Since only 8% of the SSS data coincide with precipitation data, the total bias reduces to −0.11. Hence, for all satellite SSS data points, an offset of 0.11 was added and a standard deviation of 0.34 was applied.

Appendix D: Velocity Validation

Johnson et al. [2007] found significant correlations (0.5–0.8) between the OSCAR zonal velocities and zonal velocities from moored current meters (MCMs: MCMs are a combination of mechanical current meters and mADCPs), mADCPs, drifters, and shipboard current profilers for the near-equatorial region of the Pacific. Meridional velocity is significantly less correlated compared to the correlation of the zonal velocity. The Atlantic Ocean was also examined but not shown in the paper and showed similar correlations. *Foltz et al.* [2012] found similar results at two mooring sites (4°N and 12°N) at 23°W in the equatorial North Atlantic by comparing 5 day averaged velocity data of OSCAR and MCMs. At 4°N, they found a correlation of 0.8 for the zonal velocity and no correlation for the meridional velocity.

For the equatorial mooring at 10°W, we found correlations of 0.43 for the zonal velocity and −0.1 for the meridional velocity by applying the same method as *Johnson et al.* [2007] with 5 day averaged data and using almost 13 months of upward looking mADCP profiles. Data in the upper 10–12 m of these profiles affected by surface reflections were discarded. To fill the gap of the upper 10–12 m, we extrapolated the profiles to the surface assuming constant shear. Afterward, the upper 30 m were averaged via trapezoidal integration.

The RMS of the differences was estimated with 0.21 m s^{-1} for the zonal velocity and 0.06 m s^{-1} for the meridional velocity. The same comparison for the same time period was done at the equatorial mooring at

23°W. A correlation between the zonal velocities of 0.66 and between the meridional velocities of -0.05 showed a slightly better correlation for the zonal component than at the equatorial mooring at 10°W. The RMS difference was estimated with 0.17 m s^{-1}. For the meridional velocities, a RMS of the differences of 0.03 m s^{-1} was calculated. Finally, the mean of the RMS of the differences at both sites was taken as the uncertainty for the horizontal velocities in the ACT box, leading to 0.19 m s^{-1} for the zonal velocity and 0.04 m s^{-1} for the meridional velocity. The absence of correlation for the meridional velocity at both mooring sites highlights the fact that the OSCAR velocities do not capture TIWs. In the northern box, the uncertainty estimates of *Foltz et al.* [2013] for the mooring at 4°N, 23°W were chosen, with a zonal uncertainty of 0.10 m s^{-1} and a meridional uncertainty of 0.08 m s^{-1}. They compared monthly OSCAR velocities with PIRATA currents (combination of ADCP and MCM) at three mooring sites (4°N, 11.5°N, and 20.5°N) at 23°W. They excluded the equatorial mooring, for which we found a large discrepancy between zonal velocities from OSCAR and moored observations.

References

Allen, M. R., and W. J. Ingram (2002), Constraints on future changes in climate and the hydrologic cycle, *Nature*, *419*(6903), 224–232, doi:10.1038/nature01092.

Alory, G., C. Maes, T. Delcroix, N. Reul, and S. Illig (2012), Seasonal dynamics of sea surface salinity off Panama: The far Eastern Pacific fresh pool, *J. Geophys. Res.*, *117*, C04028, doi:10.1029/2011JC007802.

Berger, M., et al. (2002), Measuring ocean salinity with ESA's SMOS mission—Advancing the science, *ESA Bull.*, *111*, 113–121.

Bingham, F. M., G. R. Foltz, and M. J. McPhaden (2012), Characteristics of the seasonal cycle of surface layer salinity in the global ocean, *Ocean Sci.*, *8*(5), 915–929, doi:10.5194/os-8-915-2012.

Bonjean, F., and G. S. E. Lagerloef (2002), Diagnostic model and analysis of the surface currents in the tropical Pacific Ocean, *J. Phys. Oceanogr.*, *32*(10), 2938–2954, doi:10.1175/1520-0485(2002)032<2938:DMAAOT>2.0.CO;2.

Bourles, B., et al. (2008), The PIRATA program: History, accomplishments, and future directions, *Bull. Am. Meteorol. Soc.*, *89*(8), 1111–1125, doi:10.1175/2008BAMS2462.1.

Boutin, J., N. Martin, Y. Xiaobin, J. Font, N. Reul, and P. Spurgeon (2012), First assessment of SMOS data over open ocean: Part II-sea surface salinity, *IEEE Trans. Geosci. Remote Sens.*, *50*(5), 1662–1675, doi:10.1109/TGRS.2012.2184546.

Boutin, J., N. Martin, G. Reverdin, X. Yin, and F. Gaillard (2013), Sea surface freshening inferred from SMOS and ARGO salinity: Impact of rain, *Ocean Sci.*, *9*(1), 183–192, doi:10.5194/os-9-183-2013.

Brandt, P., F. A. Schott, C. Provost, A. Kartavtseff, V. Hormann, B. Bourlès, and J. Fischer (2006), Circulation in the central equatorial Atlantic: Mean and intraseasonal to seasonal variability, *Geophys. Res. Lett.*, *33*, L07609, doi:10.1029/2005GL025498.

Brandt, P., G. Caniaux, B. Bourlès, A. Lazar, M. Dengler, A. Funk, V. Hormann, H. Giordani, and F. Marin (2011), Equatorial upper-ocean dynamics and their interaction with the West African monsoon, *Atmos. Sci. Lett.*, *12*(1), 24–30, doi:10.1002/asl.287.

Bumke, K., and J. Seltmann (2012), Analysis of measured drop size spectra over land and sea, *ISRN Meteorol.*, *2012*, 10 pp., doi:10.5402/2012/296575.

Bumke, K., K. Fennig, A. Strehz, R. Mecking, and M. Schröder (2012), HOAPS precipitation validation with ship-borne rain gauge measurements over the Baltic Sea, *Tellus, Ser. A*, *64*, 18486, 9 pp., doi:10.3402/tellusa.v64i0.18486.

Bumke, K., M. Schlundt, J. Kalisch, A. Macke, and H. Kleta (2014), Measured and parameterized energy fluxes estimated for Atlantic transects of R/V Polarstern, *J. Phys. Oceanogr.*, *44*(2), 482–491, doi:10.1175/JPO-D-13-0152.1.

Caniaux, G., H. Giordani, J.-L. Redelsperger, F. Guichard, E. Key, and M. Wade (2011), Coupling between the Atlantic cold tongue and the West African monsoon in boreal spring and summer, *J. Geophys. Res.*, *116*, C04003, doi:10.1029/2010JC006570.

Carton, J. A., and Z. Zhou (1997), Annual cycle of sea surface temperature in the tropical Atlantic Ocean, *J. Geophys. Res.*, *102*(C13), 27,813–27,824, doi:10.1029/97JC02197.

Da-Allada, C. Y., G. Alory, Y. du Penhoat, E. Kestenare, F. Durand, and N. M. Hounkonnou (2013), Seasonal mixed-layer salinity balance in the tropical Atlantic Ocean: Mean state and seasonal cycle, *J. Geophys. Res. Oceans*, *118*, 1–15, doi:10.1029/2012JC008357.

de Boyer Montégut, C., G. Madec, A. S. Fischer, A. Lazar, and D. Iudicone (2004), Mixed layer depth over the global ocean: An examination of profile data and a profile-based climatology, *J. Geophys. Res.*, *109*, C12003, doi:10.1029/2004JC002378.

de Boyer Montégut, C., J. Mignot, A. Lazar, and S. Cravatte (2007), Control of salinity on the mixed layer depth in the world ocean: 1. General description, *J. Geophys. Res.*, *112*, C06011, doi:10.1029/2006JC003953.

Dee, D. P., et al. (2011), The ERA-Interim reanalysis: configuration and performance of the data assimilation system, *Q. J. R. Meteorol. Soc.*, *137*(656), 553–597, doi:10.1002/qj.828.

Delcroix, T., and C. Hénin (1991), Seasonal and interannual variations of sea surface salinity in the tropical Pacific Ocean, *J. Geophys. Res.*, *96*(C12), 22,135–22,150, doi:10.1029/91JC02124.

Deser, C., A. S. Phillips, and M. A. Alexander (2010), Twentieth century tropical sea surface temperature trends revisited, *Geophys. Res. Lett.*, *37*, L10701, doi:10.1029/2010GL043321.

Dessier, A., and J. R. Donguy (1994), The sea surface salinity in the tropical Atlantic between 10°S and 30°N—Seasonal and interannual variations (1977–1989), *Deep Sea Res., Part I*, *41*(1), 81–100, doi:10.1016/0967-0637(94)90027-2.

Duing, W., P. Hisard, E. Katz, J. Meincke, L. Miller, K. V. Moroshkin, G. Philander, A. A. Ribnikov, K. Voigt, and R. Weisberg (1975), Meanders and long waves in the equatorial Atlantic, *Nature*, *257*(5524), 280–284.

Durack, P. J., and S. E. Wijffels (2010), Fifty-year trends in global ocean salinities and their relationship to broad-scale warming, *J. Clim.*, *23*(16), 4342–4362, doi:10.1175/2010JCLI3377.1.

Fairall, C. W., E. F. Bradley, J. E. Hare, A. A. Grachev, and J. B. Edson (2003), Bulk parameterization of air-sea fluxes: Updates and verification for the COARE algorithm, *J. Clim.*, *16*(4), 571–591, doi:10.1175/1520-0442(2003)016<0571:BPOASF>2.0.CO;2.

Ferrari, R., and K. L. Polzin (2005), Finescale structure of the T-S relation in the eastern North Atlantic, *J. Phys. Oceanogr.*, *35*(8), 1437–1454, doi:10.1175/JPO2763.1.

Foltz, G. R., and M. J. McPhaden (2008), Seasonal mixed layer salinity balance of the tropical North Atlantic Ocean, *J. Geophys. Res.*, *113*, C02013, doi:10.1029/2007JC004178.

Foltz, G. R., S. A. Grodsky, J. A. Carton, and M. J. McPhaden (2003), Seasonal mixed layer heat budget of the tropical Atlantic Ocean, *J. Geophys. Res.*, *108*(C5), 3146, doi:10.1029/2002JC001584.

Foltz, G. R., S. A. Grodsky, J. A. Carton, and M. J. McPhaden (2004), Seasonal salt budget of the northwestern tropical Atlantic Ocean along 38°W, *J. Geophys. Res.*, *109*, C03052, doi:10.1029/2003JC002111.

Foltz, G. R., M. J. McPhaden, and R. Lumpkin (2012), A strong Atlantic meridional mode event in 2009: The role of mixed layer dynamics, *J. Clim.*, *25*(1), 363–380, doi:10.1175/JCLI-D-11-00150.1.

Foltz, G. R., C. Schmid, and R. Lumpkin (2013), Seasonal cycle of the mixed layer heat budget in the northeastern tropical Atlantic Ocean, *J. Clim.*, *26*(20), 8169–8188, doi:10.1175/JCLI-D-13-00037.1.

Font, J., et al. (2012), SMOS first data analysis for sea surface salinity determination, *Int. J. Remote Sens.*, *34*(9-10), 3654–3670, doi:10.1080/01431161.2012.716541.

Garau, B., S. Ruiz, W. F. G. Zhang, A. Pascual, E. Heslop, J. Kerfoot, and J. Tintore (2011), Thermal lag correction on slocum CTD glider data, *J. Atmos. Oceanic Technol.*, *28*(9), 1065–1071, doi:10.1175/JTECH-D-10-05030.1.

Garraffo, Z. D., A. J. Mariano, A. Griffa, C. Veneziani, and E. P. Chassignet (2001), Lagrangian data in a high-resolution numerical simulation of the North Atlantic: I. Comparison with in situ drifter data, *J. Mar. Syst.*, *29*(1–4), 157–176, doi:10.1016/S0924-7963(01)00015-X.

Giordani, H., G. Caniaux, and A. Voldoire (2013), Intraseasonal mixed-layer heat budget in the equatorial Atlantic during the cold tongue development in 2006, *J. Geophys. Res. Oceans*, *118*, 650–671, doi:10.1029/2012JC008280.

Goes, M., G. Goni, V. Hormann, and R. C. Perez (2013), Variability of the Atlantic off-equatorial eastward currents during 1993–2010 using a synthetic method, *J. Geophys. Res. Oceans*, *118*, 3026–3045, doi:10.1002/jgrc.20186.

Gouriou, Y., and G. Reverdin (1992), Isopycnal and diapycnal circulation of the upper equatorial Atlantic Ocean in 1983–1984, *J. Geophys. Res.*, *97*(C3), 3543–3572, doi:10.1029/91JC02935.

Grodsky, S. A., J. A. Carton, and C. R. McClain (2008), Variability of upwelling and chlorophyll in the equatorial Atlantic, *Geophys. Res. Lett.*, *35*, L03610, doi:10.1029/2007GL032466.

Großklaus, M., K. Uhlig, and L. Hasse (1998), An optical disdrometer for use in high wind speeds, *J. Atmos. Oceanic Technol.*, *15*(4), 1051–1059, doi:10.1175/1520-0426(1998)015<1051:AODFUI>2.0.CO;2.

Hall, A., and S. Manabe (1997), Can local linear stochastic theory explain sea surface temperature and salinity variability?, *Clim. Dyn.*, *13*(3), 167–180, doi:10.1007/s003820050158.

Hasse, L., M. Grossklaus, K. Uhlig, and P. Timm (1998), A ship rain gauge for use in high wind speeds, *J. Atmos. Oceanic Technol.*, *15*(2), 380–386, doi:10.1175/1520-0426(1998)015<0380:ASRGFU>2.0.CO;2.

Hisard, P., and A. Morlière (1973), La terminaison du contre courant équatorial subsuperficiel Atlantique (courant de Lomonosov) dans le golfe de Guinée, *Cah. O. R. S. T. O. M., Ser. Oceanogr.*, *11*(4), 455–464.

Hosoda, S., T. Ohira, and T. Nakamura (2008), A monthly mean dataset of global oceanic temperature and salinity derived from Argo float observations, *JAMSTEC Rep. Res. Div.*, *8*, 47–59.

Hummels, R., M. Dengler, and B. Bourlès (2013), Seasonal and regional variability of upper ocean diapycnal heat flux in the Atlantic cold tongue, *Prog. Oceanogr.*, *111*, 52–74, doi:10.1016/j.pocean.2012.11.001.

Hummels, R., M. Dengler, P. Brandt, and M. Schlundt (2014), Diapycnal heat flux and mixed layer heat budget within the Atlantic Cold Tongue, *Clim. Dyn.*, doi:10.1007/s00382-014-2339-6, in press.

Jochum, M., M. F. Cronin, W. S. Kessler, and D. Shea (2007), Observed horizontal temperature advection by tropical instability waves, *Geophys. Res. Lett.*, *34*, L09604, doi:10.1029/2007GL029416.

Johns, W. E., P. Brandt, B. Bourles, A. Tantet, A. Papapostolou, and A. Houk (2014), Zonal structure and seasonal variability of the Atlantic equatorial undercurrent, *Clim. Dyn.*, 1–22, doi:10.1007/s00382-014-2136-2, in press.

Johnson, E. S., F. Bonjean, G. S. E. Lagerloef, J. T. Gunn, and G. T. Mitchum (2007), Validation and error analysis of OSCAR sea surface currents, *J. Atmos. Oceanic Technol.*, *24*(4), 688–701, doi:10.1175/JTECH1971.1.

Jouanno, J., F. Marin, Y. du Penhoat, J. Sheinbaum, and J.-M. Molines (2011a), Seasonal heat balance in the upper 100 m of the equatorial Atlantic Ocean, *J. Geophys. Res.*, *116*, C09003, doi:10.1029/2010JC006912.

Jouanno, J., F. Marin, Y. du Penhoat, J.-M. Molines, and J. Sheinbaum (2011b), Seasonal modes of surface cooling in the Gulf of Guinea, *J. Phys. Oceanogr.*, *41*(7), 1408–1416, doi:10.1175/JPO-D-11-031.1.

Kalisch, J., and A. Macke (2012), Radiative budget and cloud radiative effect over the Atlantic from ship-based observations, *Atmos. Meas. Tech.*, *5*(10), 2391–2401, doi:10.5194/amt-5-2391-2012.

Kanamitsu, M., W. Ebisuzaki, J. Woollen, S. K. Yang, J. J. Hnilo, M. Fiorino, and G. L. Potter (2002), NCEP-DOE AMIP-II reanalysis (R-2), *Bull. Am. Meteorol. Soc.*, *83*(11), 1631–1643, doi:10.1175/BAMS-83-11-1631.

Kolodziejczyk, N., B. Bourlès, F. Marin, J. Grelet, and R. Chuchla (2009), Seasonal variability of the Equatorial Undercurrent at 10°W as inferred from recent in situ observations, *J. Geophys. Res.*, *114*, C06014, doi:10.1029/2008JC004976.

Kolodziejczyk, N., F. Marin, B. Bourlès, Y. Gouriou, and H. Berger (2014), Seasonal variability of the equatorial undercurrent termination and associated salinity maximum in the Gulf of Guinea, *Clim. Dyn.*, doi:10.1007/s00382-014-2107-7, in press.

Kubota, M., A. Kano, H. Muramatsu, and H. Tomita (2003), Intercomparison of various surface latent heat flux fields, *J. Clim.*, *16*(4), 670–678, doi:10.1175/1520-0442(2003)016<0670:IOVSLH>2.0.CO;2.

Lagerloef, G. S. E., G. T. Mitchum, R. B. Lukas, and P. P. Niiler (1999), Tropical Pacific near-surface currents estimated from altimeter, wind, and drifter data, *J. Geophys. Res.*, *104*(C10), 23,313–23,326, doi:10.1029/1999JC900197.

Lagerloef, G. S. E., et al. (2008), The Aquarius/SAC-D mission: Designed to meet the salinity remote-sensing challenge, *Oceanography*, *21*(1), 68–81, doi:10.5670/oceanog.2008.68.

Lebedev, K. V., H. Yoshinari, N. A. Maximenko, and P. W. Hacker (2007), YoMaHa'07: Velocity data assessed from trajectories of Argo floats at parking level and at the sea surface, *IPRC Tech. Note*, *4*(2), 1–16.

Lee, T., G. Lagerloef, M. M. Gierach, H.-Y. Kao, S. Yueh, and K. Dohan (2012), Aquarius reveals salinity structure of tropical instability waves, *Geophys. Res. Lett.*, *39*, L12610, doi:10.1029/2012GL052232.

Legeckis, R. (1977), Long waves in the Eastern Equatorial Pacific Ocean: A view from a geostationary satellite, *Science*, *197*(4309), 1179–1181, doi:10.1126/science.197.4309.1179.

Lellouche, J. M., et al. (2013), Evaluation of global monitoring and forecasting systems at Mercator Océan, *Ocean Sci.*, *9*(1), 57–81, doi:10.5194/os-9-57-2013.

Lien, R. C., E. A. D'Asaro, and C. E. Menkes (2008), Modulation of equatorial turbulence by tropical instability waves, *Geophys. Res. Lett.*, *35*, L24607, doi:10.1029/2008GL035860.

Lumpkin, R., and S. L. Garzoli (2005), Near-surface circulation in the Tropical Atlantic Ocean, *Deep Sea Res., Part I*, *52*(3), 495–518, doi:10.1016/j.dsr.2004.09.001.

Lumpkin, R., A. M. Treguier, and K. Speer (2002), Lagrangian eddy scales in the Northern Atlantic Ocean, *J. Phys. Oceanogr.*, *32*(9), 2425–2440, doi:10.1175/1520-0485(2002)032<2425:LESITN>2.0.CO;2.

Moum, J. N., D. R. Caldwell, and C. A. Paulson (1989), Mixing in the equatorial surface layer and thermocline, *J. Geophys. Res.*, *94*(C2), 2005–2021, doi:10.1029/JC094iC02p02005.

Oakey, N. S. (1982), Determination of the rate of dissipation of turbulent energy from simultaneous temperature and velocity shear micro-structure measurements, *J. Phys. Oceanogr.*, *12*(3), 256–271, doi:10.1175/1520-0485(1982)012<0256:DOTROD>2.0.CO;2.

Osborn, T. R. (1980), Estimates of the local rate of vertical diffusion from dissipation measurements, *J. Phys. Oceanogr.*, *10*(1), 83–89, doi:10.1175/1520-0485(1980)010<0083:EOTLRO>2.0.CO;2.

Osborn, T. R., and C. S. Cox (1972), Oceanic fine structure, *Geophys. Fluid Dyn.*, *3*(1), 321–345, doi:10.1080/03091927208236085.

Perez, R. C., V. Hormann, R. Lumpkin, P. Brandt, W. E. Johns, F. Hernandez, C. Schmid, and B. Bourlès (2014), Mean meridional currents in the central and eastern equatorial Atlantic, *Clim. Dyn.*, doi:10.1007/s00382-013-1968-5, in press.

Peter, A.-C., M. Le Hénaff, Y. du Penhoat, C. E. Menkes, F. Marin, J. Vialard, G. Caniaux, and A. Lazar (2006), A model study of the seasonal mixed layer heat budget in the equatorial Atlantic, *J. Geophys. Res.*, *111*, C06014, doi:10.1029/2005JC003157.

Peters, H., M. C. Gregg, and J. M. Toole (1988), On the parameterization of equatorial turbulence, *J. Geophys. Res.*, *93*(C2), 1199–1218, doi:10.1029/JC093iC02p01199.

Philander, S. G. H. (1978), Instabilities of zonal equatorial currents, 2, *J. Geophys. Res.*, *83*(C7), 3679–3682, doi:10.1029/JC083iC07p03679.

Philander, S. G. H., and R. C. Pacanowski (1981), The oceanic response to cross-equatorial winds (with application to coastal upwelling in low latitudes), *Tellus*, *33*(2), 201–210, doi:10.1111/j.2153-3490.1981.tb01744.x.

Philander, S. G. H., D. Gu, G. Lambert, T. Li, D. Halpern, N. C. Lau, and R. C. Pacanowski (1996), Why the ITCZ is mostly north of the equator, *J. Clim.*, *9*(12), 2958–2972, doi:10.1175/1520-0442(1996)009<2958:WTIIMN>2.0.CO;2.

Prandke, H., and A. Stips (1998), Test measurements with an operational microstructure-turbulence profiler: Detection limit of dissipation rates, *Aquat. Sci.*, *60*(3), 191–209, doi:10.1007/s000270050036.

Praveen Kumar, B., J. Vialard, M. Lengaigne, V. S. N. Murty, and M. J. McPhaden (2012), TropFlux: Air-sea fluxes for the global tropical oceans—Description and evaluation, *Clim. Dyn.*, *38*(7-8), 1521–1543, doi:10.1007/s00382-011-1115-0.

Reul, N., J. Tenerelli, J. Boutin, B. Chapron, F. Paul, E. Brion, F. Gaillard, and O. Archer (2012), Overview of the first SMOS sea surface salinity products. Part I: Quality assessment for the second half of 2010, *IEEE Trans. Geosci. Remote Sens.*, *50*(5), 1636–1647, doi:10.1109/TGRS.2012.2188408.

Richardson, P. L., and G. Reverdin (1987), Seasonal cycle of velocity in the Atlantic North Equatorial Countercurrent as measured by surface drifters, current meters, and ship drifts, *J. Geophys. Res.*, *92*(C4), 3691–3708, doi:10.1029/JC092iC04p03691.

Schafstall, J., M. Dengler, P. Brandt, and H. Bange (2010), Tidal-induced mixing and diapycnal nutrient fluxes in the Mauritanian upwelling region, *J. Geophys. Res.*, *115*, C10014, doi:10.1029/2009JC005940.

Schmitt, R. W., J. R. Ledwell, E. T. Montgomery, K. L. Polzin, and J. M. Toole (2005), Enhanced diapycnal mixing by salt fingers in the thermo-cline of the tropical Atlantic, *Science*, *308*(5722), 685–688, doi:10.1126/science.1108678.

Stevenson, J. W., and P. P. Niiler (1983), Upper ocean heat budget during the Hawaii-to-Tahiti Shuttle experiment, *J. Phys. Oceanogr.*, *13*(10), 1894–1907, doi:10.1175/1520-0485(1983)013<1894:UOHBDT>2.0.CO;2.

Swenson, M. S., and D. V. Hansen (1999), Tropical Pacific ocean mixed layer heat budget: The Pacific cold tongue, *J. Phys. Oceanogr.*, *29*(1), 69–81, doi:10.1175/1520-0485(1999)029<0069:TPOMLH>2.0.CO;2.

Taylor, J. P., J. M. Edwards, M. D. Glew, P. Hignett, and A. Slingo (1996), Studies with a flexible new radiation code. II: Comparisons with air-craft short-wave observations, *Q. J. R. Meteorol. Soc.*, *122*(532), 839–861, doi:10.1002/qj.49712253204.

Tzortzi, E., S. A. Josey, M. Srokosz, and C. Gommenginger (2013), Tropical Atlantic salinity variability: New insights from SMOS, *Geophys. Res. Lett.*, *40*, 1–5, doi:10.1002/grl.50225.

von Schuckmann, K., P. Brandt, and C. Eden (2008), Generation of tropical instability waves in the Atlantic Ocean, *J. Geophys. Res.*, *113*, C08034, doi:10.1029/2007JC004712.

Wade, M., G. Caniaux, and Y. du Penhoat (2011), Variability of the mixed layer heat budget in the eastern equatorial Atlantic during 2005–2007 as inferred using Argo floats, *J. Geophys. Res.*, *116*, C08006, doi:10.1029/2010JC006683.

Wang, W. M., and M. J. McPhaden (1999), The surface-layer heat balance in the equatorial Pacific Ocean. Part I: Mean seasonal cycle, *J. Phys. Oceanogr.*, *29*(8), 1812–1831, doi:10.1175/1520-0485(1999)029<1812:TSLHBI>2.0.CO;2.

Xie, S.-P., C. Deser, G. A. Vecchi, J. Ma, H. Teng, and A. T. Wittenberg (2010), Global warming pattern formation: Sea surface temperature and rainfall, *J. Clim.*, *23*(4), 966–986, doi:10.1175/2009JCLI3329.1.

Yu, L., X. Jin, and R. A. Weller (2008), Multidecade global flux datasets from the Objectively Analyzed Air-sea Fluxes (OAFlux) project: Latent and sensible heat fluxes, ocean evaporation, and related surface meteorological variables, *OAFlux Project Tech. Rep. OA-2008-01*, pp. 1–64, Woods Hole Oceanogr. Inst, Woods Hole, Mass.